Cancer Cell

Article

Subclonal immune evasion in non-small cell lung cancer

Graphical abstract

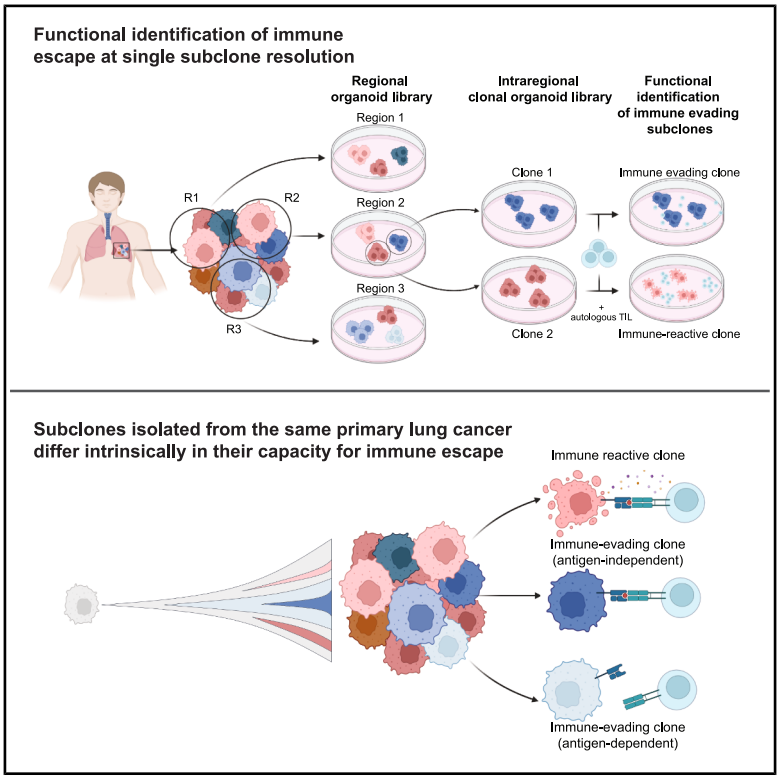

Highlights

- Organoid immune co-cultures enable identifying immune evasion at subclonal resolution
- Lung cancer subclones differ intrinsically in their capacity for immune evasion
- Subclonal evolution shapes cancer cell-intrinsic immune evasion

Authors

Krijn K. Dijkstra, Roberto Vendramin, Despoina Karagianni, ..., Sergio A. Quezada, Emile E. Voest, Charles Swanton

Correspondence

k.dijkstra@nki.nl (K.K.D.), s.quezada@ucl.ac.uk (S.A.Q.), e.voest@nki.nl (E.E.V.), charles.swanton@crick.ac.uk (C.S.)

In brief

Dijkstra et al. investigate whether individual cancer subclones differ in their immune evasion capacity. They establish organoids representing distinct subclones from multi-region lung cancer biopsies. Co-culture with T or NK cells shows heterogeneity in immune evasion across different tumor subclones, demonstrating that immune escape is shaped by subclonal evolution.

Dijkstra et al., 2025, Cancer Cell *43*, 1–17
October 13, 2025
https://doi.org/10.1016/j.ccell.2025.06.012

CellPress

Cancer Cell

CellPress
OPEN ACCESS

Article

Subclonal immune evasion in non-small cell lung cancer

Krijn K. Dijkstra,[1,2,3,4,*] Roberto Vendramin,[2,3,5] Despoina Karagianni,[3,6] Maartje Witsen,[1,4] Felipe Gálvez-Cancino,[3,6,7] Mark S. Hill,[2,3] Kane A. Foster,[6] Vittorio Barbè,[2,3] Mihaela Angelova,[2] Robert E. Hynds,[2,3,8] David R. Pearce,[2,3] Carlos Martínez-Ruiz,[2,3] James R.M. Black,[2,3] Ariana Huebner,[2,3] Oriol Pich,[2,3] Andrew Rowan,[2] Marcellus Augustine,[2,3,5,9] Clare Puttick,[2,3,10] David A. Moore,[3,11] Lydia L. Liu,[2,3] Sadegh Saghafinia,[2,3] Joris van de Haar,[1,4] Selvaraju Veeriah,[2,3] Cristina Naceur-Lombardelli,[2,3] Antonia Toncheva,[2,3] Supreet Kaur Bola,[3,6] Crispin T. Hiley,[2,3] Mariam Jamal-Hanjani,[3,12,13] Nicholas McGranahan,[3,10] Kevin Litchfield,[3,5] James L. Reading,[3,14] Benny Chain,[15,16] TRACERx consortium, Sergio A. Quezada,[3,6,17,*] Emile E. Voest,[1,4,17,*] and Charles Swanton[2,3,13,17,18,*]

[1]Department of Molecular Oncology and Immunology, the Netherlands Cancer Institute, Amsterdam, the Netherlands
[2]Cancer Evolution and Genome Instability Laboratory, The Francis Crick Institute, London, UK
[3]Cancer Research UK Lung Cancer Centre of Excellence, University College London Cancer Institute, University College London, London, UK
[4]Oncode Institute, Utrecht, the Netherlands
[5]Tumor ImmunoGenomics and Immunosurveillance Laboratory, University College London Cancer Institute, University College London, London, UK
[6]Cancer Immunology Unit, Immune Regulation and Tumor Immunotherapy Group, Research Department of Haematology, University College London Cancer Institute, London, UK
[7]Immune Regulation Laboratory, Centre for Immuno-Oncology, Nuffield Department of Medicine, University of Oxford, Oxford, United Kingdom
[8]Epithelial Cell Biology in ENT Research (EpiCENTR) Group, Developmental Biology and Cancer Department, Great Ormond Street UCL Institute of Child Health, University College London, London, UK
[9]Division of Medicine, University College London, London, UK
[10]Cancer Genome Evolution Research Group, Cancer Research UK Lung Cancer Centre of Excellence, University College London Cancer Institute, London, UK
[11]Department of Cellular Pathology, University College London Hospital, London, UK
[12]Cancer Metastasis Laboratory, University College London Cancer Institute, London, UK
[13]Department of Medical Oncology, University College London Hospitals, London, UK
[14]Pre-Cancer Immunology Laboratory, University College London Cancer Institute, London, UK
[15]University College London Cancer Institute, London, UK
[16]Division of Infection and Immunity, University College London, London, UK
[17]These authors contributed equally
[18]Lead contact
*Correspondence: k.dijkstra@nki.nl (K.K.D.), s.quezada@ucl.ac.uk (S.A.Q.), e.voest@nki.nl (E.E.V.), charles.swanton@crick.ac.uk (C.S.)
https://doi.org/10.1016/j.ccell.2025.06.012

SUMMARY

Cancers rarely respond completely to immunotherapy. While tumors consist of multiple genetically distinct clones, whether this affects the potential for immune escape remains unclear due to an inability to isolate and propagate individual subclones from human cancers. Here, we leverage the multi-region TRACERx lung cancer evolution study to generate a patient-derived organoid – T cell co-culture platform that allows the functional analysis of subclonal immune escape at single clone resolution. We establish organoid lines from 11 separate tumor regions from three patients, followed by isolation of 81 individual clonal sublines. Co-culture with tumor infiltrating lymphocytes (TIL) or natural killer (NK) cells reveals cancer-intrinsic and subclonal immune escape in all 3 patients. Immune evading subclones represent genetically distinct lineages with a unique evolutionary history. This indicates that immune evading and non-evading subclones can be isolated from the same tumor, suggesting that subclonal tumor evolution directly affects immune escape.

INTRODUCTION

Patients with non-small cell lung cancer (NSCLC) treated with immune checkpoint blockade (ICB) rarely experience complete clinical responses,[1,2] and the development of treatment strategies that achieve complete tumor remission is a major clinical challenge. The fact that for most patients, clinical response is partial at best suggests that the degree of immune pressure or sensitivity is not uniform within an individual tumor. Indeed, multi-region sampling studies reveal widespread intratumor

Please cite this article in press as: Dijkstra et al., Subclonal immune evasion in non-small cell lung cancer, Cancer Cell (2025), https://doi.org/10.1016/j.ccell.2025.06.012

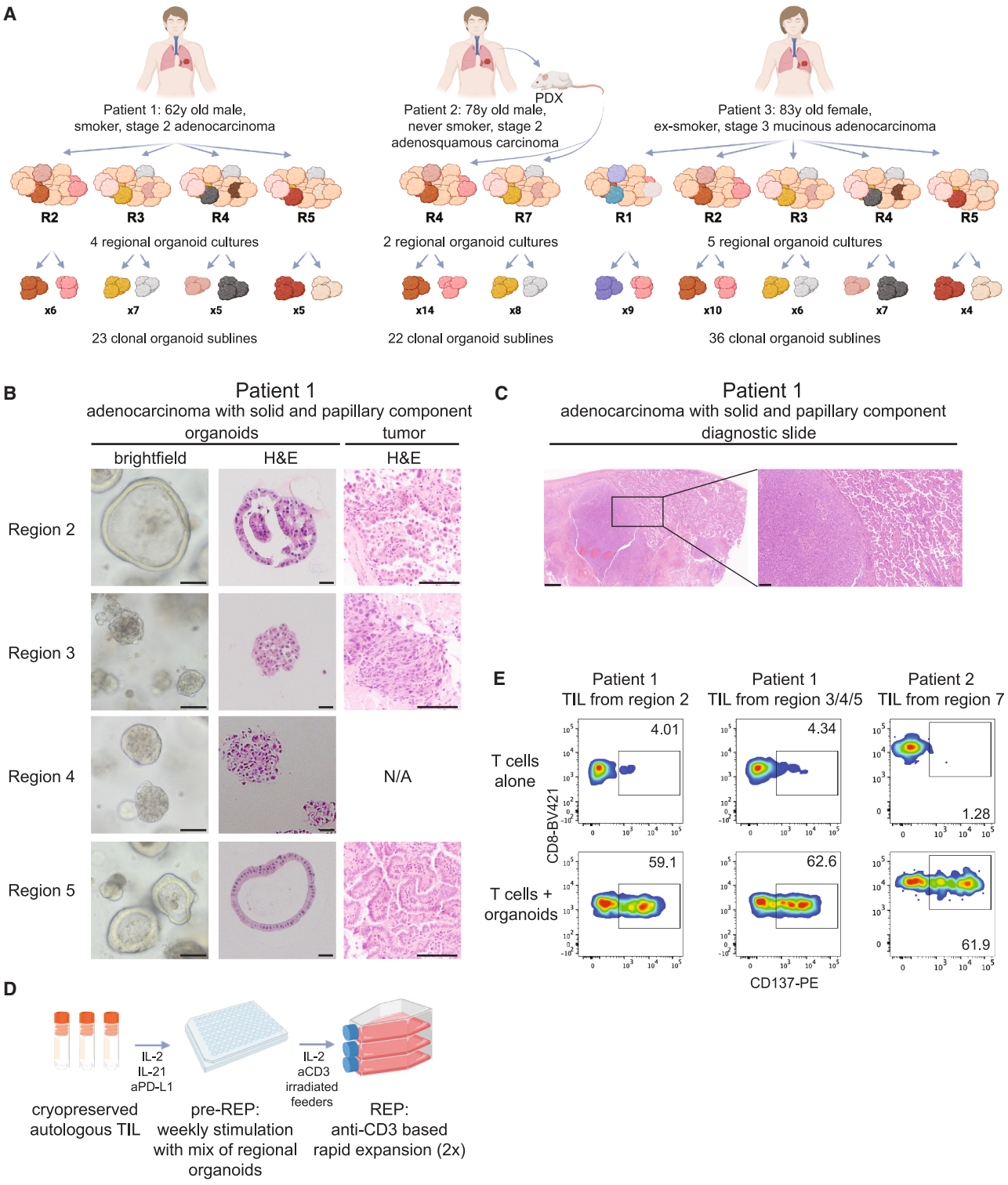

Figure 1. Establishment of a multi-region organoid T cell co-culture platform

(A) Overview of clonal organoid libraries derived from different tumor regions (created with BioRender.com).

(B) Brightfield and hematoxylin and eosin (H&E) stained slides of organoids and primary tumors from different regions from patient 1. Scale bar: 100 μm.

(C) H&E stained diagnostic slide of the lung cancer from patient 1. Scale bar: 1 mm (left panel) or 250 μm (right panel).

(legend continued on next page)

Please cite this article in press as: Dijkstra et al., Subclonal immune evasion in non-small cell lung cancer, Cancer Cell (2025), https://doi.org/10.1016/j.ccell.2025.06.012

heterogeneity of anti-tumor immunity, with different tumor regions showing substantial differences in the degree of immune cell infiltration, expression of neoantigens, and T cell receptor (TCR) repertoire.[3–5] Local immune escape is likely to have profound clinical consequences, and tumors with more than one "cold" region (poorly infiltrated by immune cells) have a particularly poor prognosis.[6]

However, the mechanistic basis of incomplete tumor clearance remains largely unknown. Local variation in anti-tumor immunity can be driven by cancer-extrinsic differences, such as stromal barriers impeding immune cell access, immunosuppressive microenvironments, or T cell exhaustion.[7,8] As genomic instability and branching tumor evolution result in genetically heterogeneous tumors,[9,10] immune escape can also be driven by inherent differences in immune evasion capacity between cancer subclones. These different mechanisms are difficult to resolve using descriptive data alone.

Genomic approaches, particularly those combined with multi-region sampling or spatial imaging, allow the assessment of particular subclones with specific immune contexts.[4,8,11,12] However, it remains challenging to infer the functional immune evasion capacity of individual cancer subclones from purely descriptive data. The absence of mutations in a set of relevant immune genes is no guarantee that a cancer cell cannot evade immunosurveillance through other (perhaps unstudied) means. Therefore, it has so far been challenging to determine the extent to which individual cancer subclones differ in their functional capacity for immune evasion, due to an inability to isolate and propagate individual tumor subclones from human cancers to functionally evaluate their immunogenicity.

Recent advances in organoid culture have made it possible to establish patient-derived tumor organoid lines that capture genetic diversity at the clonal level.[13] We previously developed an autologous organoid – T cell co-culture system to determine the interaction between cancer cells and T cells at the level of an individual patient.[14] Here, we leverage the multi-region TRACERx lung cancer evolution study to generate a patient-derived study platform that allows the evaluation of T cell responses to individual cancer subclones. TRACERx is a prospective study based on multi-region sampling of primary and metastatic NSCLC.[10] We used this to generate parallel organoid sublines from spatially distinct tumor regions and from separate clones within individual regions, and to evaluate their capacity to elicit an immune response in co-cultures with autologous tumor infiltrating lymphocytes (TILs) or donor-derived natural killer (NK) cells. The integration of patient-derived functional assays with an in-depth characterization based on DNA, RNA and T cell receptor (TCR) sequencing allowed the direct and functional demonstration of immune escape at the level of single subclones. These results (1) show that individual cancer subclones differ intrinsically in their capacity for immune evasion and (2) provide an approach to prospectively identify and isolate immune evading subclones from cancer patients. This suggests that subclonal cancer evolution continues to sculpt the immune evasive properties of cancer cells.

RESULTS

Establishment of a multi-region organoid T cell co-culture platform

We hypothesized that individual tumor subclones would differ intrinsically in their capacity to evade immune pressure. To test this hypothesis, we developed a fully autologous multi-region organoid-T cell co-culture platform. First, organoids were established from multiple spatially separated tumor regions from NSCLC patients in the TRACERx study, followed by handpicking of individual organoids to capture both inter- and intraregion heterogeneity.[10] We generated clonal organoid libraries from three different patients, consisting of a total of 81 clonal sublines and 11 distinct regional lines (Figure 1A; Table S1). Organoids from the three patients differed in morphology, in agreement with the different histological growth patterns of the original tumors (Figures 1B, S1A, and S1B). Patient 1 showed histological heterogeneity within the tumor,[15] which was recapitulated in the multi-region organoid cultures from this patient (Figures 1B and 1C).

We then expanded autologous patient TIL by weekly stimulation with a mixture of all regional organoids from that patient, mixed at equal ratios (pre-rapid expansion protocol; pre-REP) (Figure 1D). For patient 1, two different sources of TILs were available, originating from different tumor regions. After pre-REP for patients 1 and 2, TILs were highly reactive to a mixture of regional tumor organoids (Figures 1E and S1C). Limited TILs were available from patient 3, and their numbers further decreased during the pre-REP, precluding testing of tumor reactivity. We therefore focused on the two patients for which tumor-reactive TILs were available. We further expanded TILs to large numbers in two cycles of stimulation with anti-CD3 antibodies, irradiated feeders and high dose IL-2 (REP) (Figure 1D; Table S2).[16] Taken together, we established multi-region clonal organoid libraries for three patients, combined with a biobank of expanded tumor-reactive autologous TILs for two patients.

To further characterize the expanded TIL products, we performed bulk TCR beta chain (TCRb) sequencing. Expanded TILs from patient 1 showed an oligoclonal TCRb repertoire, with 5–8 of the most expanded clones comprising 75% of the population (Figure S1D). The two different sources of TILs (derived from either region 2 (R2), or R3/4/5 combined) contained both clones that were unique or shared between the two TIL products (Figures S1E and S1F). In contrast, for patient 2 the TCRb repertoire consisted of a dominant clone comprising >90% of expanded TILs (Figure S1G). To trace this clone back to the original tumor, we performed single-cell RNA sequencing of unexpanded TILs, directly isolated from the corresponding tumor fragments. The dominant clone in our expanded TIL product was also the most abundant T cell clone in unexpanded TILs (Figure S1G). Furthermore, this clone showed high expression

(D) Workflow for expansion of tumor-reactive TIL. REP: rapid expansion phase.
(E) Flow cytometry plots of TIL reactivity (after pre-REP) upon stimulation with a mixture of dissociated regional autologous tumor organoids. Numbers indicate percentage of tumor-reactive $CD8^+$ T cells expressing CD137.
See also Figure S1, Tables S1, and S2.

Please cite this article in press as: Dijkstra et al., Subclonal immune evasion in non-small cell lung cancer, Cancer Cell (2025), https://doi.org/10.1016/j.ccell.2025.06.012

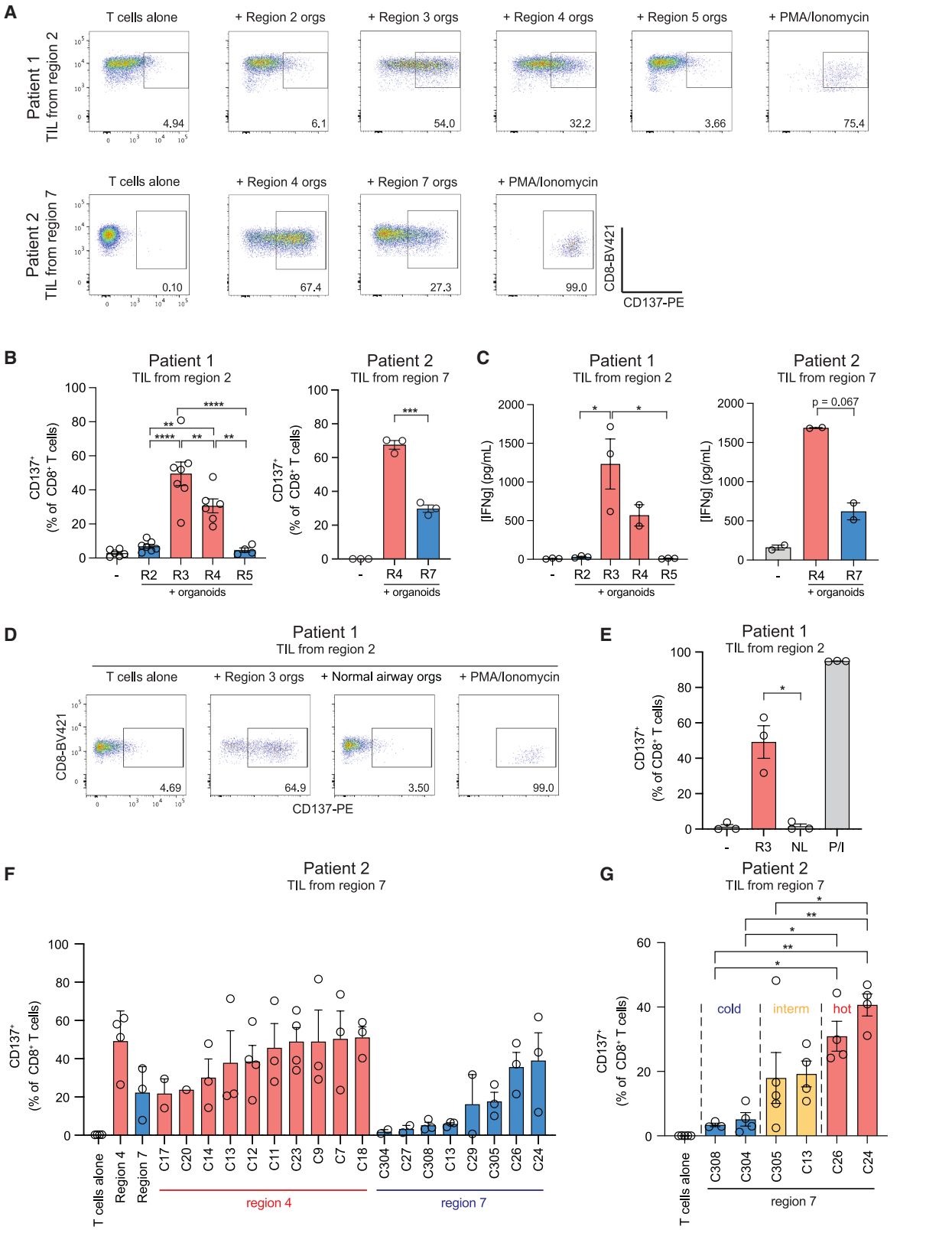

Figure 2. Tumor-intrinsic T cell evasion capacity differs both between and within tumor regions

(A) Reactivity of expanded TILs upon stimulation with dissociated autologous tumor organoids.

(B) Quantification of (A). Patient 1: mixed-effects model (n = 4–7); patient 2: paired t-test (*n* = 3).

(legend continued on next page)

of markers associated with CD8$^+$ T cell exhaustion, and scored high on a signature associated with neoantigen-reactive T cells (neoTCR score) (Figures S1H and S1I).[17] This suggests that our protocol resulted in the expansion of a single highly abundant and previously exhausted tumor-reactive T cell clone from this patient. Of note, the subdominant (7.8%) T cell clone in expanded TIL mapped back to a naive CD4$^+$ T cell population with low neoTCR score (Figures S1H and S1I). We did not observe CD4$^+$ T cell reactivity against organoids from this patient, suggesting this may be an expanded bystander clone.[18,19]

Tumor-intrinsic T cell evasion capacity differs both between and within tumor regions

Having observed that expanded TILs were reactive against mixtures of regional organoid lines, we next assessed whether T cell reactivity differed between organoids derived from different tumor regions. Recognition assays of expanded TILs with individual organoid sublines revealed strong differences between organoids derived from separate regions in their capacity to elicit a T cell response (Figures 2A–2C, S2A, and S2B; Table S1). For patient 1, organoids from R3 and R4 induced strong T cell recognition, while organoids from R2 and R5 resulted in limited T cell activation above baseline (Figures 2A–2C). The two different TIL products for patient 1 showed broadly similar patterns of reactivity, with neither showing strong reactivity toward the "cold" organoids R2 and R5. The two TIL products differ in their reactivity toward organoids from R4, which was less strongly recognized by TILs derived from R3/4/5 (Figures 2B, 2C, S2A, and S2B). Commonalities as well as differences between the two TIL products were also seen at the level of the tumor-reactive TCRb repertoire (of CD8$^+$CD137$^+$ T cells upon organoid co-culture), with some tumor-reactive clonotypes shared between both TIL products, but also several large tumor-reactive clones that had expanded considerably less in one of both products (Figures S1E and S1F). In patient 2, TILs also differed in their response to regional organoids, with organoids from R4 inducing >2-fold more T cell activation than organoids from R7 (Figures 2A–2C). T cell activation by organoids was MHC-I-dependent (Figure S2C) and not induced by matched normal airway organoids (available for patient 1; Figures 2D and 2E), indicating the T cell response is tumor-specific.

Individual NSCLC regions can differ in their clonal complexity, consisting of one or multiple separate subclones.[10] To determine whether the capacity for immune evasion not only differs between, but also within regions, we screened our clonal organoid libraries for recognition by autologous TIL. For patient 1, variation in organoid-induced T cell activation was largely region-dependent, with limited differences between organoid sublines derived from the same region (Figure S2D). In contrast, for patient 2 we observed pronounced differences in the capacity for immune evasion between different clonal lines from the same tumor region. This was most obvious for parallel sublines established from R7 (Figure 2F). We confirmed our initial, library-wide screen with more focused assays for six sublines from R7 with diverging T cell evasion capacity, which we classified as "cold" (immune evading), "intermediate", or "hot" (Figure 2G). Reactivity toward mixtures of hot and cold organoids was similar to the average reactivity of separate hot and cold organoids, suggesting that (in this experimental setting) the immune evasion phenotype of cold clones was largely cell-autonomous and did not exert a dominant effect on the reactivity toward hot clones in a mixture (Figure S2E). Collectively, these data indicate that tumors harbor distinct tumor cell subpopulations with the intrinsic capacity to evade T cell recognition, and that this heterogeneity can be present both across and within tumor regions.

Immune-evading and non-evading tumor subpopulations represent genetically distinct subclones

To determine whether organoid sublines that differed in immune evasion capacity represented distinct genetic lineages, we integrated whole exome sequencing (WES) data of regional and/or intraregional organoid sublines and their original tumor regions to generate phylogenetic trees (Figures 3A–3B, S3A and S3B). For patient 1, organoids and corresponding tumor regions mapped to the same major branch of the phylogenetic tree (Figure 3A). Regions corresponding to immune evasive and non-evasive organoids (Figure 2B) mapped to different major branches that diverged after the most recent common ancestor (MRCA), suggesting that subclones with different T cell evasion capacities diverged early during tumor evolution. This was also reflected in strong divergence of hot and cold organoids at the single nucleotide variant (SNV) level, with more SNVs shared between organoid lines of the same immune class (either hot *or* cold) than SNVs observed in the common trunk (both hot *and* cold) (Figure 3C).

For patient 2, the organoid phylogenetic tree consisted of two major branches that tracked with the two different tumor regions, but no additional branches that separated hot and cold organoid sublines (Figures 3B, S3A, and S3B). This was not entirely unexpected, since for this patient hot and cold organoids were isolated by handpicking individual organoids from within one region, rather than between spatially separated tumor regions. As phylogenetic trees are constructed based on the degree of SNV sharing between clones, the relatively low number of clone-specific mutations detected by WES (Figure S3C) may have limited our ability to identify phylogenetic relationships between organoid sublines beyond the regional level.

(C) Quantification of secreted IFNg in supernatant of co-cultures from Figure 2B (n = 2–3, depending on supernatant availability). Patient 1: mixed-effects model. Patient 2: paired t-test.
(D) Reactivity of expanded TILs upon stimulation with autologous tumor or normal airway organoids.
(E) Quantification of (D). Paired t-test (n = 3). NL: normal airway organoids; P/I: PMA/Ionomycin.
(F) TIL reactivity upon stimulation of expanded TILs with regional or clonal organoid lines from patient 2 (n = 1–4).
(G) As (F), for selected clonal sublines from R7. Mixed effects model (n = 3–5).
Error bars in panels B, C, E, F, and G show mean ± S.E.M. Numbers in panels A and D indicate percentage of CD8$^+$ T cells expressing CD137. Asterisks indicate significance: *$p < 0.05$; **$p < 0.01$; ***$p < 0.001$; ****$p < 0.0001$.
See also Figures S1, S2, and Table S1.

Please cite this article in press as: Dijkstra et al., Subclonal immune evasion in non-small cell lung cancer, Cancer Cell (2025), https://doi.org/10.1016/j.ccell.2025.06.012

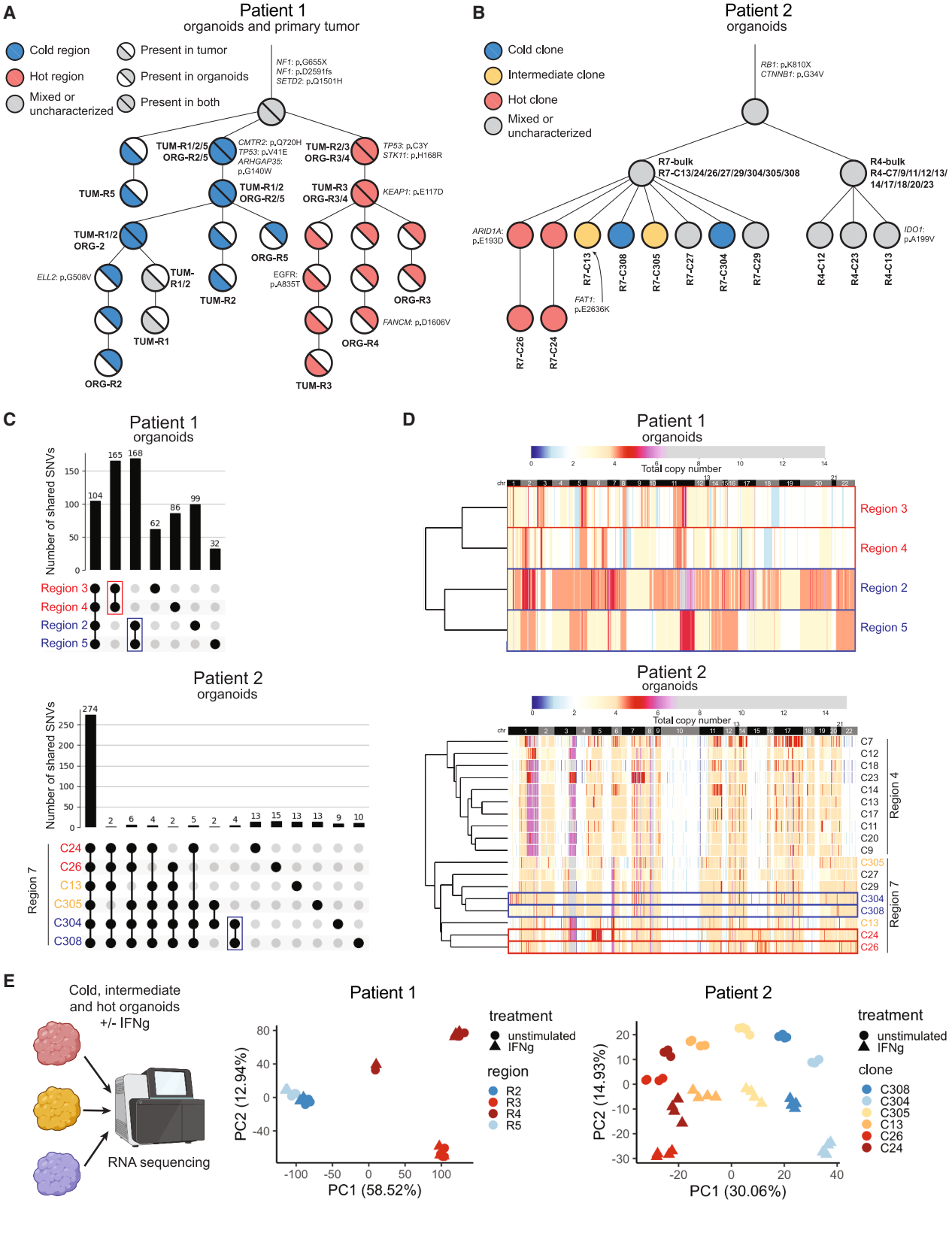

(legend on next page)

Please cite this article in press as: Dijkstra et al., Subclonal immune evasion in non-small cell lung cancer, Cancer Cell (2025), https://doi.org/10.1016/j.ccell.2025.06.012

To determine whether any genetic relationships between cold sublines in patient 2 may have been obscured by the stringency of our thresholds to define mutational clusters (≥5 SNVs per cluster in Figure S3C), we relaxed our thresholds to ≥2 SNVs per cluster, revealing four mutations that were exclusively present in cold clones (Figure 3C). Of these mutations, three were either synonymous, intronic, or present in a gene not expressed in organoids (Table S3). The remaining SNV was a non-synonymous mutation in *NOA1*. We determined that *NOA1* levels did not contribute to the immune evasion potential of these organoids using siRNA-mediated knockdown (Figures S3D and S3E). Therefore, these mutations are unlikely to be the driver of the immune evasion phenotype.

Unsupervised hierarchical clustering based on organoid copy number alterations (CNAs) showed that for both patients immune evasion capacity is associated with distinct genetic lineages, with hot and cold organoid sublines forming separate clusters (Figure 3D). While cold and hot clones from patient 2 differ by few SNVs (Figure 3C), their distinct CNAs (Figure S3F) complement the SNV data and show that cold clones from this patient form a distinct genetic lineage from the hot clones, primarily defined by chromosomal alterations.

Regional organoids from patient 1 differed genetically more from each other than regional organoids from patient 2 (Figure S3G), in line with the more striking difference in T cell response to regional organoids for patient 1. Organoids from these patients shared most, though not all, of the mutations present in the original tumor (Figure S3H); some divergence could be because the regional biopsy was divided into different segments that were used for DNA sequencing or organoid culture and therefore were not fully identical, or due to selective outgrowth of subclones during model establishment.

We then performed RNA sequencing to determine whether hot and cold organoids were not only genetically distinct but also diverged at the transcriptional level (Figure 3E). Hot, intermediate and cold organoids strongly separated along the first principal component, mirroring the hierarchy in their ability to induce a T cell response, both in the absence and presence of interferon gamma (IFNg) (Figure 3E). This indicates that these subclonal lineages have undergone a major rewiring of their transcriptome, which was also apparent from the >1000 differentially expressed genes between cold and hot clones (Table S4; Figure S4A). Plotting organoid lines from both patients in the same principal component analysis (PCA) indicated that the principal components (PC) associated with immune evasion did not overlap between the two patients (compare PC2 and PC3 in Figure S4B), suggesting that these patients use different routes toward immune evasion. Pathways enriched in hot or cold clones are shown in Figure S4C.

Although the response to IFNg was less pronounced in hot compared to cold organoids from patient 1 (Figures S4D–S4F), the difference in T cell activation between organoid lines was similar regardless of whether organoids were pre-stimulated with IFNg or not (Figures 2B and S5A), suggesting that an altered response to IFNg did not underlie the differences in the ability to induce a T cell response in our assays.

Taken together, the association of immune evasion capacity with genomic and transcriptomic divergence of subclones suggests that these tumors, at some point during their evolutionary history, have diverged into distinct subpopulations with unique immune evasion phenotypes. This shows that tumor evolution can give rise to genetically and transcriptionally distinct clones that differ intrinsically in their capacity to evade T cell pressure.

Identification of subclonal immune evasion by both antigen-dependent and -independent mechanisms

Cancers can use diverse immune evasion strategies, which can be broadly divided into antigen-dependent mechanisms (e.g., loss of MHC-I, other components of the antigen processing machinery, or the target antigen itself) and antigen-independent mechanisms (e.g., induction of inhibitory checkpoints, secretion of immunosuppressive factors).[20] To determine whether the subclonal immune evasion mechanisms operating in the cold clones in our study were antigen-dependent or -independent, we made use of a matched TCR-antigen system (Figure 4A).[21,22] Healthy donor T cells were transduced with a TCR specific to the model antigens NY-ESO-1 or MART-1, which could be exogenously loaded onto organoids from both patients, which expressed the *HLA-A2:01* allele (Table S5). We reasoned that antigen-independent mechanisms of immune evasion should similarly affect organoid recognition by autologous TILs and model antigen-specific T cells; however, antigen-dependent immune evasion should be rescued upon loading of the cognate antigen for TCR-transduced T cells.

In contrast to the almost complete lack of recognition of R2 and R5 organoids by autologous TILs from patient 1 (Figure 2B), recognition of peptide-loaded R2 and R5 organoids by NY-ESO-1 specific T cells was not reduced compared to hot (R3 and R4) organoids (Figure 4B). Surprisingly, organoids from R3 were also recognized by NY-ESO-1 T cells in the absence of peptide loading (Figure S5B), suggesting endogenous (and subclonal) expression of this antigen, which was confirmed by RNA sequencing and qPCR (Figures S5C and S5D). We therefore also performed recognition experiments with MART-1 as an alternative target antigen (which was not

Figure 3. Immune evading and non-evading tumor subpopulations represent genetically distinct subclones

(A and B) Phylogenetic tree based on primary tumor regions and corresponding regional organoid lines (patient 1, (A)), or of clonal and regional organoid lines (patient 2, (B)). Colors indicate immunophenotype based on co-culture data. Nodes labeled by the represented primary tumor region or organoid lines. Non-synonymous exonic mutations in lung cancer drivers or immune evasion genes (Methods) indicated.

(C) UpSet plots indicating the number of single nucleotide variants (SNVs) shared between regional (patient 1) or intraregional (patient 2) organoid sublines. Minimum number of SNVs per group is 5 (patient 1) or 2 (patient 2). SNVs unique to either hot or cold sublines are marked by red and blue outlines, respectively.

(D) Unsupervised hierarchical clustering of copy number profiles of different regional (patient 1) or intraregional clonal (patient 2) organoid lines. Hot and cold sublines marked by red and blue outlines, respectively. Colors in heatmap indicate total copy number for chromosomal segments across the genome.

(E) Principal component analysis (PCA) of RNA sequencing data of regional (patient 1) or intraregional clonal (patient 2) organoid lines ± IFNg for 24h (n = 4 per organoid line). Axes indicate percentage of variance explained by corresponding principal component. Created with BioRender.com.

See also Figures S3–S6, and Tables S3 and S4.

Please cite this article in press as: Dijkstra et al., Subclonal immune evasion in non-small cell lung cancer, Cancer Cell (2025), https://doi.org/10.1016/j.ccell.2025.06.012

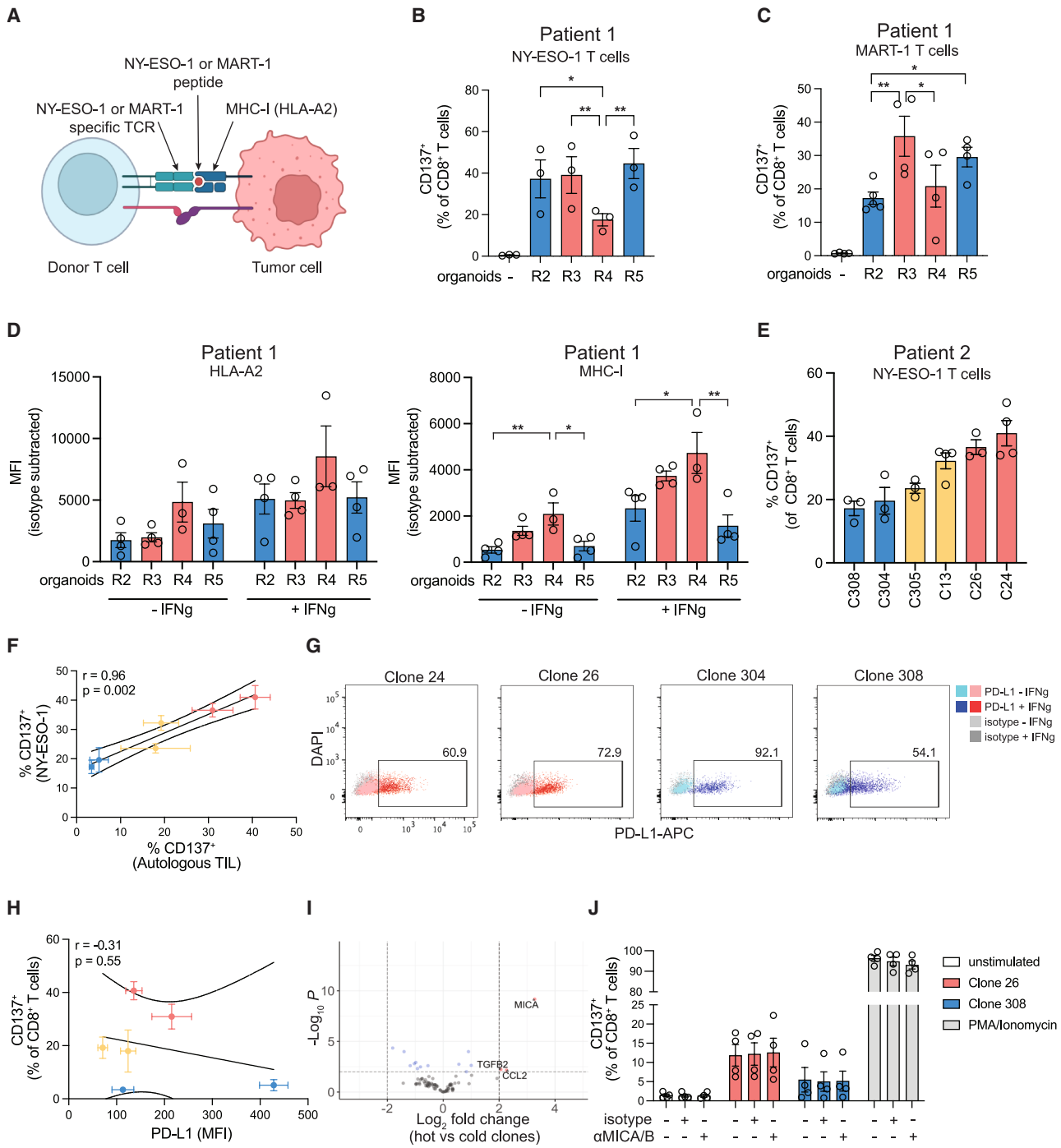

Figure 4. Subclonal immune evasion is mediated by both antigen-dependent and -independent mechanisms

(A) Matched antigen-TCR system. Created with BioRender.com.

(B) Reactivity of NY-ESO-1-specific T cells against regional organoids loaded with NY-ESO-1 peptide (repeated measures ANOVA, $n = 3$).

(C) As in (B), using MART-1-specific T cells (mixed effects model; n = 4–5).

(D) Organoid cell surface expression of HLA-A2 or pan-MHC-I protein (± IFNg for 24h) determined by flow cytometry. MFI: median fluorescence intensity. One-way ANOVA (performed separately for conditions ± IFNg; n = 3–4).

(E) Reactivity of NY-ESO-1-specific T cells against NY-ESO-1-loaded clonal organoid lines. Results of mixed-effects analysis (n = 3–4) in Table S6.

(F) Pearson correlation between reactivity of autologous expanded TILs (Figure 2G; n = 3–5) and NY-ESO-1-specific T cells (Figure 4E; n = 3–4) with regression line and 95% confidence intervals.

(G) Flow cytometry plots of cell surface PD-L1 expression gated on live tumor cells (± IFNg for 24h). Numbers indicate percentage of PD-L1$^+$ tumor cells upon IFNg stimulation.

(legend continued on next page)

endogenously expressed by these organoids (Figure S5C)), confirming that reactivity against cold organoids could be rescued in matched antigen-T cell systems (Figures 4C and S5B). The model antigens in these assays were added as peptides to the culture supernatant and can bind directly to MHC-I molecules, bypassing the antigen processing machinery (APM). To rule out that the limited recognition of cold organoids is due to APM defects, we transduced organoids with full-length NY-ESO-1 protein, which led to a similar recognition of NY-ESO-1^{+} hot (R3) and cold (R5) organoids (Figures S5E–S5H), suggesting that the APM is functional in these organoids. Cell surface expression of HLA-A2 proteins was comparable between hot and cold organoids (Figure 4D), and cold organoids did not show any genomic loss or transcriptional repression of HLA class I genes that could account for lack of recognition (Figures S5I and S5J). While pan-MHC-I cell surface expression levels were lower in cold organoids, pre-incubation of organoids with IFNg increased MHC-I expression to levels comparable to (unstimulated) hot organoids (Figure 4D) but did not restore the capacity of cold organoids to induce a T cell response (Figure S5A). This suggests that differences in MHC-I expression levels or APM dysfunction do not explain the lack of T cell recognition of cold organoids. Overexpression of NY-ESO-1 in cold clones did not result in activation of autologous TIL indicating that this is not the target antigen of autologous TIL (data not shown).

In contrast to patient 1, for patient 2, clones that were poorly recognized by autologous TIL also showed limited capacity to stimulate NY-ESO-1 T cells in a matched antigen-T cell system (Figures 4E, 4F, and S6A; Table S6). MHC-I and HLA-A2 expression levels were not consistently higher for hot versus cold clones (Figures S6B–S6D), suggesting that immune evasion is due to antigen-independent mechanisms.

Collectively, we identify subclonal immune escape based on both antigen-dependent (patient 1) and antigen-independent (patient 2) mechanisms. The observation that for patient 1, the dominant factor driving subclonal immune evasion was antigen-dependent suggests that the transcriptional differences between these regions (Figure 3E) may either affect processes that have limited impact on T cell evasion in the context of our assays, or directly affect antigenicity e.g., through transcriptional repression of neoantigens.[4] Of note, the number of predicted neoantigens that are unique to cold (R2/5) or hot (R3/4) organoids was more than 3x as high as the number of neoantigens shared across all regions (Figure S6E), indicating that these clones show highly different antigen landscapes at the genetic level. These data indicate that subclonal immune escape can be identified across different settings, involving both antigen-dependent or -independent mechanisms, and that organoid T cell co-culture platforms allow differentiating between these mechanisms.

Limited prediction of subclonal immune evasion by genomic or transcriptomic approaches

We identified immune evading subclones based on a direct functional readout, i.e., their capacity to induce an autologous T cell response. Analysis of most patient cohorts typically does not include functional assays and instead relies on computational approaches to identify immune evading subclones. We therefore determined whether the immune evading subclones from these patients could be identified based on their genomic or transcriptomic characterization alone.

We explored several genomic features associated with immune evasion. The number of non-synonymous SNVs or insertions/deletions (indels) was similar between hot and cold clones (Figure S6F). We determined whether cold clones showed any mutations in a curated list of genes involved in immune recognition or evasion (Table S7) and annotated this to the phylogenetic trees (Figures 3A and 3B). Patient 1 showed no potentially inactivating mutations in this gene set. This patient did show subclonal mutations in *KEAP1* and *STK11* (Figure 3A) which have been associated with immune evasion,[23,24] but these mutations were present in hot rather than cold clones, suggesting that they did not impair tumor cell-intrinsic T cell recognition in our system. Patient 2 contained a clonal mutation in *CTNNB1* (present in all clones) (Figure 3B), as well as a mutation in *CXCL2* that was only present in cold clones but was unlikely to contribute to the immune evasion phenotype as RNA sequencing showed no expression of *CXCL2* in these organoids (Table S3 and data not shown). As in patient 1 (Figures S5I and S5J), cold clones from patient 2 also did not show any genomic loss or transcriptional repression of HLA class I genes compared to hot clones (Figures S6G and S6H). Taken together, DNA sequencing did not reveal any alterations that pointed to the immune evasion phenotype of the cold subclones that were identified in a functional manner.

Since for patient 2 the mechanism of subclonal immune escape was antigen-independent (Figures 4E and 4F), we determined whether phenotypic characterization of its cold organoid sublines could have predicted their immune evasion capacity. PD-L1 was not expressed under baseline conditions, and IFNg led to a limited induction of expression that did not correlate with T cell reactivity (Figures 4G, 4H, and S6I). We then performed differential gene expression analysis on RNA sequencing data of cold and hot clones (Table S4) and assessed whether cold clones could be identified based on differences in expression of immune evasion genes (Table S7). Of this panel, three genes (*MICA*, *TGFB2*, and *CCL2*) were significantly differentially expressed between cold and hot clones (Figure 4I; Table S4). However, T cell-evading clones could not unambiguously be identified based on this expression pattern, as both *TGFB2* and *CCL2* are best known for their immunosuppressive functions[25,26] yet were overexpressed in hot rather than cold clones.

(H) Pearson correlation between reactivity of autologous expanded TIL (Figure 2G; n = 3–5) and PD-L1 MFI (Figure S6I; n = 3–4) with regression line and 95% confidence intervals.

(I) Differentially expressed genes involved in immune control (Table S7) between hot and cold organoid sublines of patient 2. *p* values based on differential expression analysis using limma voom and adjusted using the Benjamini-Hochberg method.

(J) Reactivity of expanded TILs toward organoid lines ± MICA/B blocking antibodies or isotype controls ($n = 4$).

Error bars in panels B, C, D, E, F, H and J show mean ± S.E.M. Asterisks indicate significance: $^{*}p < 0.05$; $^{**}p < 0.01$; $^{***}p < 0.001$; $^{****}p < 0.0001$.

See also Figures S5, S6, Tables S3, S4, S5, S6, and S7.

Please cite this article in press as: Dijkstra et al., Subclonal immune evasion in non-small cell lung cancer, Cancer Cell (2025), https://doi.org/10.1016/j.ccell.2025.06.012

Furthermore, while *MICA* (upregulated in hot clones) can act as a co-stimulatory ligand for T cells through the NKG2D receptor,[27] blocking MICA did not affect T cell recognition of organoids (Figure 4J).

Taken together, a comprehensive genetic and transcriptomic characterization alone would have been insufficient to identify the T cell evading subclones that were identified using functional approaches. This underscores the challenge in determining subclonal immune evasion based on descriptive data alone and highlights the added value of functional study platforms to determine the impact of tumor heterogeneity on immune evasion.

Regional composition of the immune microenvironment

Our finding that individual cancer subclones differed intrinsically in their ability to evade T cell pressure was made possible by our reductionist co-culture system. In an actual tumor, cancer cells reside in more complex microenvironments which may further impact their sensitivity to immune effectors. We therefore evaluated the local immune composition of the tumors from which our organoids were derived using multiplex immunofluorescence. In patient 1, tumor R2 and R5 (the source of T cell-evading organoids) showed relatively structured nests of tumor cells, in contrast to tumor R3 (non-T cell-evading organoids) with extensive necrosis, disorganized areas of tumor cells, and less uniform pan-cytokeratin (PanCK) staining (Figure 5). R3 showed a neutrophilic infiltrate, although neutrophils were also present to some extent in R2 and R5. T cell infiltration was present in all tumor regions without obvious differences, aside from a prominent CD8 infiltrate in the upper (more necrotic) tumor area of R3. Interestingly, although macrophages were present both in R3 and R5 (less prominently in R2), in R5 these remained restricted to stromal areas and did not infiltrate the tumor nests. In contrast, in R3, abundant macrophages were found directly interspersed with tumor cells. Therefore, for this patient, different tumor regions were associated with distinct microenvironments.

The two regions (R4 and R7) from patient 2 were largely comparable, with multiple patches of necrosis (Figure S7). Strikingly, a lymphoid and myeloid immune infiltrate was present in these tumor areas, but largely restricted to necrotic or stromal areas, with very little infiltration into the tumor bed. Similarly, for patient 3, cancer cells grew in isolated nests (in line with its mucinous adenocarcinoma histology), with T cells, isolated NK cells and myeloid cells predominantly in stromal areas, with limited infiltration into the tumor islands.

In our functional experiments, we have singled out one form of immune escape (the ability to impair a T cell response) to provide proof of concept that this inherently differs across individual cancer subclones within one tumor. Characterization of the tumor microenvironment suggests that these subclones resided in highly complex microenvironments. Although these data remain at this point descriptive, this suggests that additional layers of immune escape may be present, e.g., by restricting immune cell entry into the tumor area.

Subclonal heterogeneity in the capacity for NK cell recognition

For patient 3, we could not isolate and expand sufficient TILs for functional studies. As an alternative, we therefore challenged regional organoids from patient 3 with healthy donor-derived NK cells. We observed significant heterogeneity in the ability of regional organoids to induce NK cell activation, with organoids from R5 resulting in markedly less NK cell activation compared to other regions (Figures 6A and 6B; Table S1). Reconstruction of the tumor phylogeny shows that while R1-R4 share a common branch, R5 falls on a separate branch, indicating its distinct evolutionary history (Figure 6C). This was further supported by mapping of driver gene alterations on the phylogenetic tree, which showed that R1-4 contained a mutation in *FANCM* and *B2M* (a subunit of MHC-I), which was absent in R5. Given that MHC-I levels are an important determinant of NK cell activation, with high expression acting as an inhibitory signal,[28] we determined whether MHC-I cell surface expression differed between regional organoids. Organoids from R5 showed significantly higher MHC-I cell surface expression (Figure 6D), and the potential of organoids to stimulate NK cells was strongly negatively correlated with MHC-I expression (Figure 6E). Together, this shows that while escape from autologous T cells could not be assessed, in this patient, cancer subclones populating different tumor regions differed in their capacity for recognition by NK cells. This provides evidence for subclonal escape from immune effectors in all 3 patients investigated in this study, across three different settings (antigen-dependent and -independent escape from T cells, and escape from NK cells).

DISCUSSION

Why most lung cancers that respond to immunotherapy show a partial, but not complete, response is still largely unclear. Immunological heterogeneity can be driven both by cancer-extrinsic factors,[8] or by intrinsic differences between cancer subclones in their ability to withstand immune cell pressure. Here, we investigated the latter and show that parallel organoid sublines, representing tumor subclones from the same patient, show substantial variation in their capacity to elicit a T cell or NK cell response, despite being cultured under identical conditions over multiple passages. This suggests that the subclonal immune evasion identified here is cell-intrinsic, heritable and at least to some extent fixed. Indeed, hot and cold organoid sublines represent genetically and transcriptionally distinct subclones with a unique evolutionary history. ‘‘Fixed’’ and ‘‘plastic’’ immune evasion mechanisms are not necessarily mutually exclusive, and it will be relevant to determine whether specific environmental conditions (e.g., hypoxia) could override any intrinsic heterogeneity in immune evasion capacity. In addition, technologies that allow associating immune microenvironments with specific subclones will provide a more refined view of the association between clonal heterogeneity and local immune evasion.[12,29]

The extent to which immune escape mechanisms evolve early (i.e., clonally, shared between all cancer cells) or late in tumor evolution is a matter of ongoing debate,[4,9,11] although data from TRACERx suggest that a substantial proportion of HLA LOH events in early-stage, treatment-naive NSCLC are subclonal in nature.[30] Here we show that subclonal diversification significantly affects the magnitude of the T cell response elicited by different cancer subclones. These data suggest that, at least in early-stage, treatment-naive, lung cancers, evolutionary forces acting after the last clonal sweep can still shape relevant

Please cite this article in press as: Dijkstra et al., Subclonal immune evasion in non-small cell lung cancer, Cancer Cell (2025), https://doi.org/10.1016/j.ccell.2025.06.012

CellPress
OPEN ACCESS

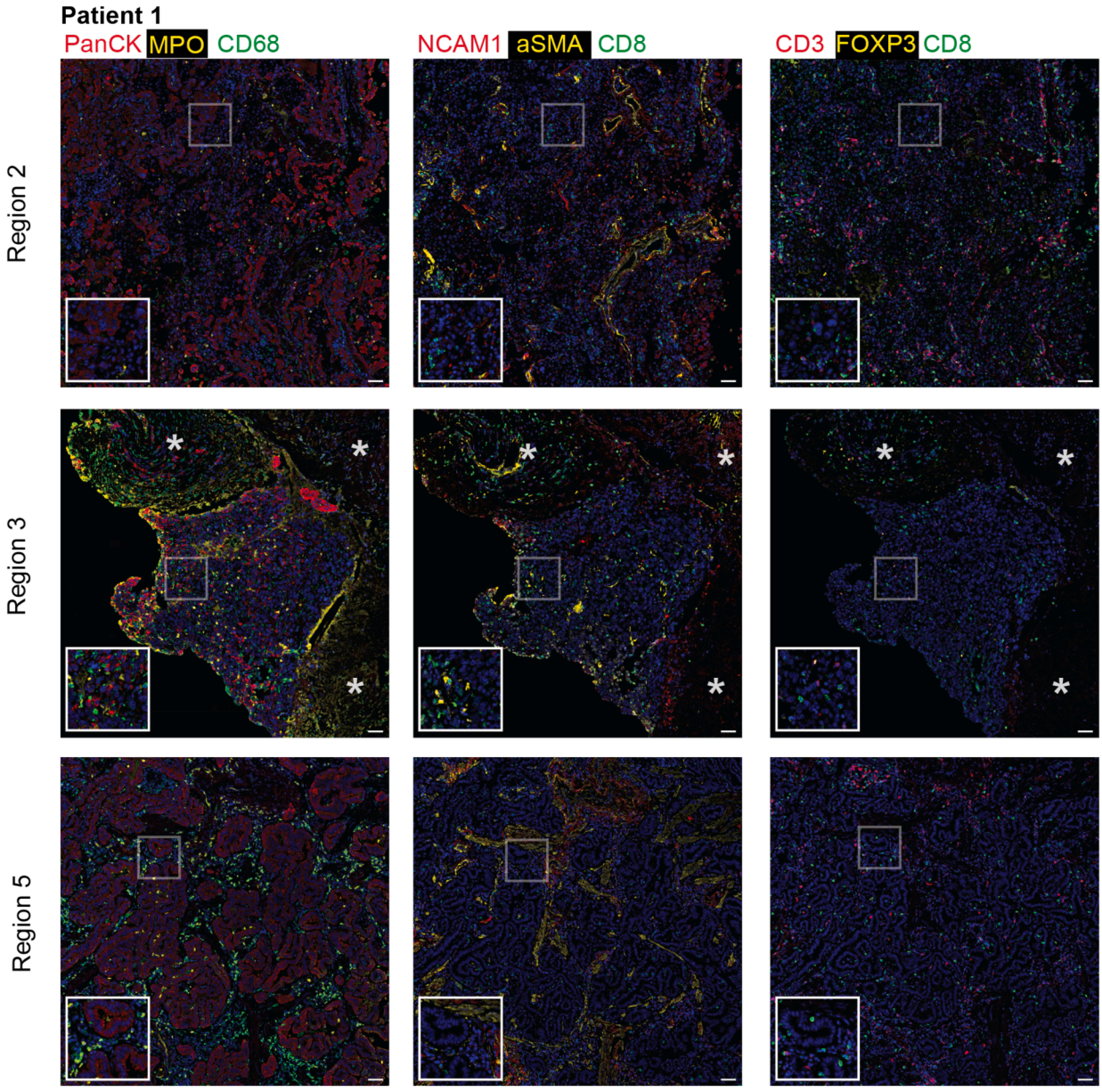

Figure 5. Regional composition of the immune microenvironment

Composite images showing multiplex immunofluorescence staining of serial sections of different tumor regions from patient 1. Asterisks indicate necrosis. Signal thresholds were kept constant for individual markers across different samples, except for CD68 in R2 which showed markedly lower intensity and was adjusted to reach a similar signal-to-noise ratio. panCK: pan-cytokeratin (epithelial cells); MPO: myeloperoxidase (neutrophils); CD68 (macrophages); NCAM1: neural cell adhesion molecule 1 (NK cells); aSMA: alpha-smooth muscle actin (fibroblasts); CD3 (T cells); FOXP3: forkhead box P3 (regulatory T cells); CD8 (cytotoxic T cells). Scale bar: 200 μm. Lower left insets are 2× magnified corresponding to the boxed area. No FFPE slide available for R4.
See also Figure S7.

interactions between cancer cells and immune cells. We find evidence of subclonal escape from immune effectors in all 3 patients in widely divergent contexts (both antigen-dependent and -independent escape from T cells, and escape from NK cells).

Despite their comprehensive characterization, we could not have identified the immune evading subclones based on descriptive (e.g., genetic or transcriptomic) data alone. This underscores the challenge in attributing functional properties, such as immune evasion, to specific subclones in clinical datasets. Immune evasion may be overestimated (e.g., alterations in immune genes that have limited functional consequence), as well as underestimated (as shown here by immune escape of subclonal organoid lines despite absence of any canonical immune evasion alterations). This warrants some degree of caution in interpreting purely descriptive datasets in the absence of further

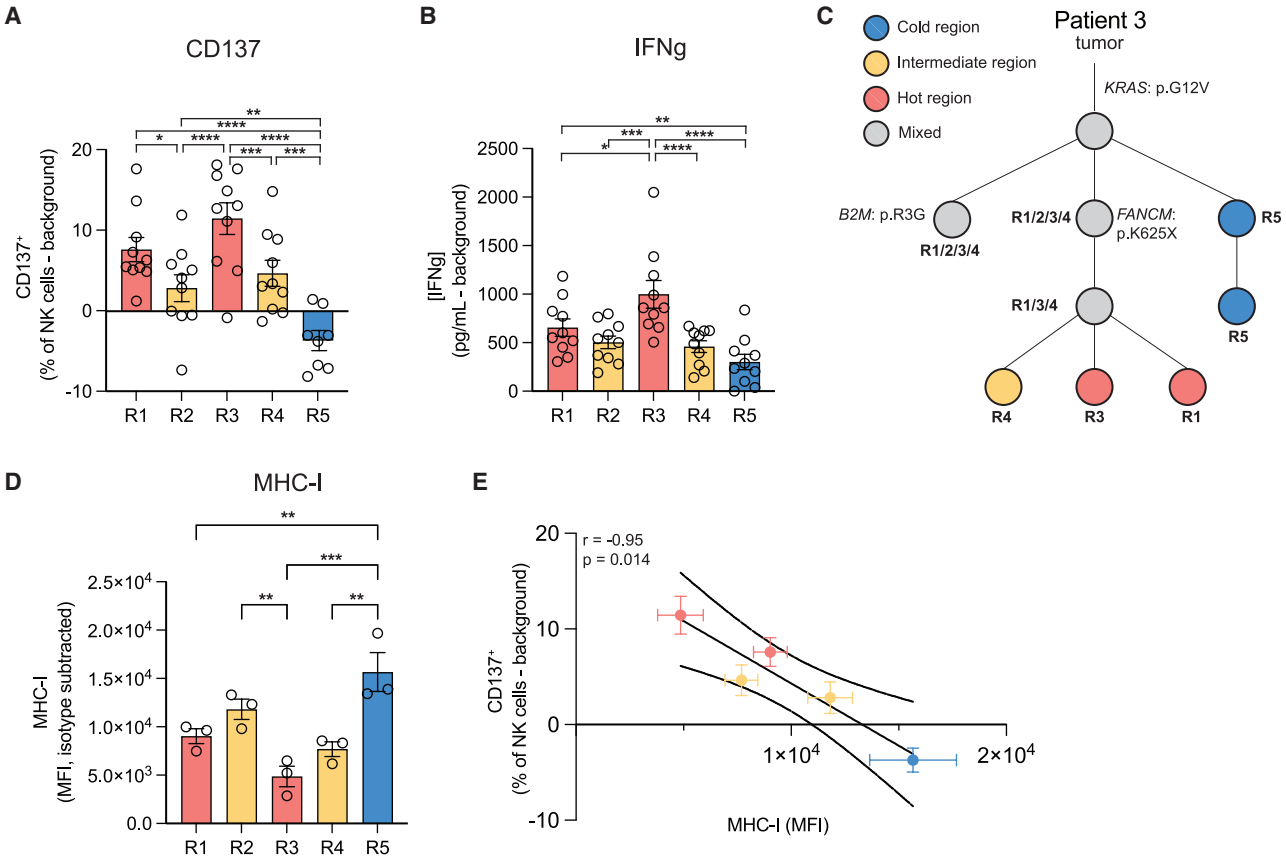

Figure 6. Subclonal heterogeneity in the capacity for NK cell recognition

(A) NK cell reactivity upon co-culture with regional tumor organoids from patient 3, with background CD137 expression (unstimulated) subtracted. Circles indicate individual data points from different NK cell donors ($n = 4$) across different replicate experiments ($n = 5$). Mixed-effects model (n = 8–10) with experiment and donor as random effects; Bonferroni corrected p-values.

(B) Quantification of secreted IFNg in supernatant of experiments in Figure 6A. Circles indicate individual data points from different NK cell donors ($n = 4$) across different replicate experiments ($n = 5$). Mixed-effects model ($n = 10$) with experiment and donor as random effects; Bonferroni corrected p-values.

(C) Phylogenetic tree of primary tumor regions. Colors indicate immunophenotype based on co-culture data. Nodes labeled with the represented primary tumor region. Exonic non-synonymous mutations in lung cancer drivers or immune evasion genes (STAR Methods) indicated alongside corresponding nodes.

(D) Organoid cell surface expression of pan-MHC-I protein. MFI: median fluorescence intensity. Repeated-measures ANOVA ($n = 3$).

(E) Pearson correlation between cell surface MHC expression (from panel D; $n = 3$) and CD137 induction (with background CD137 expression of unstimulated NK cells subtracted; from panel A; n = 8–10) with regression line and 95% confidence intervals.

Error bars in panels A, B, D, and E show mean ± S.E.M. Asterisks indicate significance: $^{*}p < 0.05$; $^{**}p < 0.01$; $^{***}p < 0.001$; $^{****}p < 0.0001$.

See also Table S1.

functional evidence. While not always feasible, this also highlights the added value of incorporating functional platforms into the design of clinical studies.

Our data suggest that subclonal tumor evolution continues to shape important cellular phenotypes, including the escape from immune effectors, and that both immune-evading and non-evading clones can be isolated from the same tumor. It will be relevant to assess the functional implications of such heterogeneity, and longitudinal sampling of primary tumors and matched metastases, coupled to functional co-culture platforms, may help to determine the relationship between subclonal immune evasion capacity and the ability to seed metastases.[31,32] It is also important to note that all tumor organoids in our study are derived from treatment naive patients and therefore reflect subclonal immune evasion mechanisms likely selected for during the evolution of the tumor in the absence of immune/cytotoxic or targeted therapy. Taken together, the establishment of clonal organoid libraries and their use in functional T cell co-cultures has allowed the demonstration of the existence of immune evasion in human cancers at single subclone resolution. Ultimately, we anticipate that this will allow the mapping of various routes that heterogeneous lung cancers have evolved toward immune evasion, and the design of therapeutic strategies aimed at complete tumor remission.

Limitations of the study

The reductionist nature of our co-culture platform makes it possible to specifically dissect the impact of intratumor heterogeneity on the recognition of cancer cells by $CD8^{+}$ T cells. This represents only one element of the cancer-immune interface,

and co-culture systems including other immune or stromal cells[33,34] may be of value to determine whether the same subclones that escape CD8$^+$ T cell pressure are also able to withstand pressure from other immune effectors.

The limited number of patients studied here prevents us from determining to what extent cancer cell-intrinsic subclonal immune evasion is a more universal phenomenon. This limitation is largely driven by the challenge of generating multi-region organoid libraries from lung cancers with matched autologous TILs. The low establishment rate of lung cancer organoids is a known challenge in the field,[35–37] and our study presents the additional complexity of requiring subclonal organoid derivation from several distinct regions from the same tumor. We attempted organoid culture from a total of 42 patients, or 166 individual tumor regions. For 7 patients, organoids were established from at least one tumor region (success rate of 17%, in line with previous studies),[35] but for only 4 of these 7 patients could organoids be established from multiple regions. Three of these patients are presented here; the fourth patient was not studied further as organoids strongly decreased their proliferation rate after several passages, which limited the possibility to perform functional studies. This highlights the complexity of generating multi-region clonal organoid libraries for lung cancer and at the same time underscores the unique nature of this cohort. Further technological innovations to improve organoid derivation rates are required to determine the extent of cancer cell-intrinsic subclonal immune evasion across larger cohorts of patients.

RESOURCE AVAILABILITY

Lead contact

Requests for further information and resources should be directed to and will be fulfilled by the lead contact, Charles Swanton (Charles.Swanton@crick.ac.uk).

Materials availability

Biological materials generated in this study, including organoids and expanded TILs, are available through the Cancer Research UK & University College London Cancer Trials Centre (ctc.tracerx@ucl.ac.uk) for non-commercial research purposes. Access will be granted upon review of a project proposal by a TRACERx data access committee and upon entering into an appropriate data access agreement, subject to any applicable ethical approvals and availability of stocks.

Data and code availability

Sequencing data of organoids, PDX samples, primary tumor regions and T cells from the TRACERx study used during this study have been deposited with the European Genome–phenome Archive (EGA), which is hosted by The European Bioinformatics Institute (EBI) and the Center for Genomic Regulation (CRG) under dataset accession code EGAD00001015537. Access is controlled by the TRACERx data access committee and details regarding applications for access are available on the relevant EGA page. Exome sequencing data of the primary tumor[10] and PDX model[38] from CRUK0718 have been published before.

Processed DNA, RNA, and TCR sequencing data (from the TRACERx study) used during this study, and code for its analysis, have been deposited at Zenodo, which is maintained by CERN that serves as a platform for sharing and preserving datasets, under https://doi.org/10.5281/zenodo.11520198.

CONSORTIA

TRACERx consortium members: Abigail Bunkum, Adam Atkin, Aiman Alzetani, Akshay J Patel, Alan Kirk, Alexander James Procter, Alexander M Frankell, Alexandra Rice, Allan Hackshaw, Amrita Bajaj, Anand Devaraj, Anca Grapa, Andrew G Nicholson, Andrew Kidd, Andrew Rowan, Angela Dwornik, Angela Leek, Angeliki Karamani, Anne-Marie Hacker, Anshuman Chaturvedi, Antonio Paiva-Correia, Aoife Walker, Apostolos Nakas, Ariana Huebner, Arjun Nair, Asia Ahmed, Aya Osman, Azmina Sodha-Ramdeen, Babu Naidu, Benny Chain, Camilla Pilotti, Carla Castignani, Carlos Martínez-Ruiz, Caroline Dive, Catarina Veiga, Charles Swanton, Charles-Antoine Collins-Fekete, Chiara Proli, Chris Bailey, Cian Murphy, Claire Wilson, Clare E Weeden, Clare Puttick, Claudia Lee, Colin R Lindsay, Corentin Richard, Craig Dick, Crispin T Hiley, Cristina Naceur-Lombardelli, Daniel Kaniu, David A Moore, David Chuter, David Lawrence, David R Pearce, Davide Patrini, Dean A Fennell, Despoina Karagianni, Dionysis Papadatos-Pastos, Ekaterini Boleti, Elaine Borg, Elizabeth Keene, Emilia L Lim, Emilie Martinoni Hoogenboom, Emma Colliver, Emma Nye, Eric Lim, Erik Sahai, Eustace Fontaine, Eva Grönroos, Felice Granato, Fiona H Blackhall, Fleur Monk, Francesco Fraioli, Francisco Gimeno-Valiente, Gareth A Wilson, Gary Middleton, Gary Royle, George Kassiotis, Georgia Moth, Georgia Stavrou, Gerald Langman, Gerasimos-Theodoros Mastrokalos, Gillian Price, Gurdeep Matharu, Hanyun Zhang, Harshil Bhayani, Heather Cheyne, Helen L Lowe, Helen Shackleford, Hemangi Chavan, Hilgardt Raubenheimer, Hugo JWL Aerts, Ieva Usaite, Imran Noorani, Jack Davies Hodgkinson, Jack French, Jacki Goldman, Jacqui A Shaw, James L Reading, James RM Black, James W Holding, James Wilson, Jason F Lester, Jayant K Rane, Jeanette Kittel, Jennifer Whiteley, Jerome Nicod, John A Hartley, John Le Quesne, Jonas Demeulemeester, Jonathan Tugwood, Judith Cave, Juliette Novasio, Junaid Choudhary, Karen Grimes, Karl S Peggs, Katey S S Enfield, Katherine D Brown, Kayalvizhi Selvaraju, Kayleigh Gilbert, Keith M Kerr, Kendadai Rammohan, Kerstin Haase, Kerstin Thol, Kevin G Blyth, Kexin Koh, Khalid AbdulJabbar, Kristiana Grigoriadis, Krupa Thakkar, Kunal Bhakhri, Leah Ensell, Leena Joseph, Lily Robinson, Lucrezia Patruno, Lyn Ambrose, Madava Djearaman, Madeleine Hewish, Magali N Taylor, Mairead MacKenzie, Maise Al Bakir, Mandeesh Sangha, Mansi Shah, Maria Chiara Pisciella, Maria Litovchenko, Maria Zagorulya, Mariam Jamal-Hanjani, Martin D Forster, Mary Falzon, Mathew Carter, Mathew Thomas, Matthew G Krebs, Michael J Shackcloth, Michalina Magala, Michelle M Leung, Mickael Escudero, Mihaela Angelova, Miklos Diossy, Mo Asif, Mohamad Tufail, Mohammed Khalil, Molly Scotland, Monica Sivakumar, Mpho Malima, Nadia Fernandes, Neal Navani, Nicholas McGranahan, Nicola Totton, Nicolai J Birkbak, Nikos Kostoulas, Nnennaya Kanu, Olivia Lucas, Oriol Pich, Pat Gorman, Patricia Georg, Paul Ashford, Paul Bishop, Paulo De Sousa, Pedro Oliveira, Peter Russell, Peter Van Loo, Philip Crosbie, Philip Hobson, Piotr Pawlik, Pratibha Shah, Rachel Rosenthal, Rebecca Boyles, Reena Khiroya, Richard Kevin Stone, Ricky M Thakrar, Rija Zaidi, Robert Bentham, Robert CM Stephens, Roberto Salgado, Roberto Vendramin, Rocco Bilancia, Roland F Schwarz, Sadegh Saghafinia, Salomey Kellet, Sam M Janes, Samuel Gamble, Sara Waplington, Sarah Benafif, Sarah Booth, Sarah Danson, Sean Dulloo, Selvaraju Veeriah, Seng Kuong Anakin Ung, Serena Chee, Sergio A Quezada, Sharon Vanloo, Shirley Richardson, Sian Harries, Silviu I Buderi, Simon Jordan, Simone Zaccaria, Siow Ming Lee, Sofina Begum, Sonya Hessey, Sophia Ward, Sridhar Rathinam, Stefan Boeing, Stephan Beck, Steve Bandula, Supreet Kaur Bola, Takahiro Karasaki, Tamara Denner, Tanya Ahmad, Teresa Marafioti, Theepan Visakan, Thomas B K Watkins, Thomas Patrick Jones, Tom L Kaufmann, Tracey Cruickshank, Victoria Spanswick, Vijay Joshi, Vittorio Barbè, Wei-Ting Lu, William Hill, Wing Kin Liu, Xiaoxi Pan, Yien Ning Sophia Wong, Yin Wu, Yinyin Yuan, Yutaka Naito, Yvonne Summers, Zainab Kalokoh, Zoe Ramsden, Zoltan Kaplar, Zoltan Szallasi.

ACKNOWLEDGMENTS

The TRACERx study (ClinicalTrials.gov: NCT01888601) is sponsored by University College London (UCL/12/0279). TRACERx is funded by Cancer Research UK (C11496/A17786) and is coordinated through the Cancer Research UK and UCL Cancer Trials Center, which receives core funding from CRUK (C444/A15953). We are grateful to the patients and relatives who participated in the TRACERx study, and all site personnel, investigators, funders and industry partners who supported the generation of the data within this study. We thank staff at the Genomics, Cell Services, Experimental Histopathology, and Flow Cytometry facilities at the Francis Crick Institute, as well as the flow cytometry facility and core facility molecular pathology & biobanking (CFMPB) at the Netherlands Cancer Institute for lab support. We

acknowledge Marg Crawford and Vicky Dearing for their contributions in exome library preparation and sequencing.

This work was supported by the Cancer Research UK Lung Cancer Centre of Excellence, the CRUK City of London Centre Award (C7893/A26233) and the UCL Experimental Cancer Medicine Centre.

We thank Manar Shafat, Gordon Weng-Kit Cheung, Martin Pule and Angeliki Karamani for help with generation of NY-ESO-1 specific T cells; Ton Schumacher, John Haanen and Wouter Scheper for provision of MART-1 specific T cells; Manuel Varas-Godoy for designing and kindly sharing the NY-ESO-1 expression constructs; Vincent Pappalardo for statistical support; and Marije Kuiken for assistance in data acquisition. Indicated images and graphical abstract are created with BioRender.com.

K.K.D. was supported by funding from the European Union's Horizon 2020 research and innovation programme under the Marie Skłodowska-Curie grant agreement No. 101024529, a ZonMW Rubicon fellowship (no. 452020102), and a ZonMW Veni fellowship (no. 09150162210100).

R.V. and K.L. are funded by the UK Medical Research Council (MR/V033077/1), the Rosetrees Trust and Cotswold Trust (A2437), the Royal Marsden Cancer Charity (thanks to the Ross Russell family and Macfarlanes donations), Melanoma Research Alliance and Cancer Research UK (C69256/A30194).

A.R. is funded by The Francis Crick Institute.

M.A. was supported by the Momentum Fellowship from the Mark Foundation for Cancer Research (24-008-FSH).

J.L.R. is supported by a Future Leaders Fellowship award from the UK Research and Innovation Medical Research Council (UKRI MRC grant number MR/W011786/1) a Cancer Research UK (CRUK) early detection project award (CRUK; EDDPJT-Nov22/100042), a CRUK Biology to prevention award (PRCBTP-Nov23/100012) a CRUK City of London PhD studentship (CANCTA-2022/100001), a National Institute for Health Research University College London Hospitals Biomedical Research Centre award [NIHR UCL BRC; BRC907/CN/JR/101330], a consortium award from the International Alliance for Cancer Early Detection [CRUK ACED; ACEPGM-2022/10000], MRC-DTP PhD studentships (MR/N013867/1), an HRH National Scholarship of Thailand PhD award and a UCL Philanthropic Percy Steven's PhD Fellowship.

B.C. was supported by Cancer Research UK, the Rosetrees Trust and the UCLH Biomedical Research Centre.

M.J-H has received funding from CRUK, NIH National Cancer Institute, IASLC International Lung Cancer Foundation, Lung Cancer Research Foundation, Rosetrees Trust, UKI NETs and NIHR.

R.E.H. was supported by the CRUK Lung Cancer Centre of Excellence and was a Wellcome Trust Sir Henry Wellcome Fellow (WT209199/Z/17/Z).

S.A.Q. is funded by a Cancer Research UK (CRUK) Senior Cancer Research Fellowship (C36463/A22246), and both S.A.Q. and D.K. are funded by a CRUK Biotherapeutic Program grant (C36463/A20764). S.A.Q. and F.G.-C. were supported by a Cancer Research UK Brain Tumour Award (A28592). F.G.-C. is funded by a Kidani Advance Training Fellowship at the University of Oxford. S.K.B. is supported by the CRUK City of London Centre Award (CANCTA-2023/100002). This work was undertaken at UCL with support from the CRUK-CoL Centre (C7893/A26233).

E.E.V. is supported by core funding from Oncode Institute.

C.S. is a Royal Society Napier Research Professor (RSRP\R\210001). His work is supported by the Francis Crick Institute that receives its core funding from Cancer Research UK (CC2041), the UK Medical Research Council (CC2041), and the Wellcome Trust (CC2041). For the purpose of Open Access, the author has applied a CC BY public copyright licence to any Author Accepted Manuscript version arising from this submission. C.S. is funded by Cancer Research UK (TRACERx (C11496/A17786), PEACE (C416/A21999) and CRUK Cancer Immunotherapy Catalyst Network); Cancer Research UK Lung Cancer Centre of Excellence (C11496/A30025); the Rosetrees Trust, Butterfield and Stoneygate Trusts; Novo Nordisk Foundation (ID16584); Royal Society Professorship Enhancement Award (RP/EA/180007 & RF\ERE\231118)); National Institute for Health Research (NIHR) University College London Hospitals Biomedical Research Centre; the Cancer Research UK-University College London Centre; Experimental Cancer Medicine Centre; the Breast Cancer Research Foundation (US) (BCRF-22-157); Cancer Research UK Early Detection an Diagnosis Primer Award (Grant EDDPMA-Nov21/100034); and The Mark Foundation for Cancer Research Aspire Award (Grant 21-029-ASP) and ASPIRE Phase II award (Grant 23-034-ASP). CS is in receipt of an ERC Advanced Grant (PROTEUS) from the European Research Council under the European Union's Horizon 2020 research and innovation programme (grant agreement no. 835297).

AUTHOR CONTRIBUTIONS

K.K.D. conceived the study, designed and performed experiments and analyses, and wrote the manuscript. R.V. designed and performed experiments and analyses, contributed to the design of the study, and contributed to writing the manuscript. D.K. and F.G.-C. assisted with T cell experiments and advised on immunological aspects of the study. Mihaela Angelova analyzed multiplex immunofluorescence data. M.S.H., A.H., S.S., and L.L.L. performed genomic analyses. K.A.F. performed TCR sequencing analyses. V.B. assisted with organoid establishment. R.E.H. and D.R.P. provided PDX samples. J.R.M.B., C.M.-R., O.P., Marcellus Augustine, and J. v.d.H. assisted with transcriptomic analyses. C.M.-R. reviewed computational code. A.R. and M.W. performed experiments. C.P. performed analyses of HLA LOH. D.A.M. assisted with pathology review. S.V., C.N.-L., A. T., and S.K.B. coordinated sample acquisition and patient recruitment. C. T.H. supported acquisition of clinical data. M.J.-H. and C.S. coordinated patient recruitment and follow-up, and designed, oversaw, and led the clinical study. N.M. and K.L. assisted with genomic analyses. J.L.R. and S.A.Q. assisted with immunological analyses. B.C. oversaw and assisted with TCR sequencing analyses. E.E.V. supervised the work at the Netherlands Cancer Institute. S.A.Q. and C.S. jointly supervised the work at the Francis Crick Institute and University College London.

DECLARATION OF INTERESTS

K.K.D. provided consultancy services to Achilles Therapeutics UK Ltd.

R.V. declares research funding from CRUK TDL–Ono–LifeArc alliance and Genesis Therapeutics.

K.L. has a patent on indel burden and CPI response pending and speaker fees from Roche tissue diagnostics, research funding from CRUK TDL–Ono–LifeArc alliance, Genesis Therapeutics, and consulting roles with Ellipses Pharma, Monopteros, Tempus, Saga Diagnostics, and Kynos Therapeutics. K.L. is a current employee of Isomorphic Labs.

C.P. holds a patent pending in determining HLA disruption (PCT/EP2023/059039).

J.v.d.H. received research funding from Sanofi S.A. outside this work.

D.A.M. reports speaker fees from AstraZeneca, Eli Lilly, BMS and Takeda, consultancy fees from AstraZeneca, Thermo Fisher, Takeda, Amgen, Janssen, MIM Software, Bristol-Myers Squibb, and Eli Lilly and has received educational support from Takeda and Amgen.

C.T.H. received speaker fees from AstraZeneca and Merck, research funding from Roche, Astra Zeneca and UCLH NIHR BRC, and has a paid advisory role for GenesisCareUK.

E.E.V. is founder and current member of the supervisory board of the Hartwig Medical Foundation, independent non-executive director of Sanofi, co-founder of Mosaic Therapeutics, and board member and founder of the Center for Personalized Cancer Treatment. He has received clinical study grants from Amgen, AstraZeneca, BI, BMS, Clovis, Eli Lilly, GSK, Ipsen, MSD, Novartis, Pfizer, Roche, and Sanofi.

J.L.R. reports speaker fees from Boehringer Ingelheim and GlaxoSmithKline, consults for Achilles Therapeutics Ltd and has filed patents for T cell driven cancer early detection (PCT/EP2023/076521 and PCT/EP2023/076511).

M.J.-H. has consulted for Astex Pharmaceuticals, Pfizer and Achilles Therapeutics, and is a member of the Achilles Therapeutics Scientific Advisory Board and Steering Committee, has received speaker honoraria from Pfizer, Astex Pharmaceuticals, Oslo Cancer Cluster, Bristol Myers Squibb, Genentech and GenesisCare. M.J.-H is listed as a co-inventor on a European patent application relating to methods to detect lung cancer (PCT/US2017/028013), this patent has been licensed to commercial entities and, under terms of employment, M.J.-H. is due a share of any revenue generated from such license(s), and is also listed as a co-inventor on the GB priority

patent application (GB2400424.4) with title: Treatment and Prevention of Lung Cancer.

N.M. has stock options in and has consulted for Achilles Therapeutics and holds a European patent in determining HLA LOH (PCT/GB2018/052004), a patent pending in determining HLA disruption (PCT/EP2023/059039), and is a co-inventor to a patent to identify responders to cancer treatment (PCT/GB2018/051912).

S.A.Q. is a founder, CSO, and holds stock options of Achilles Therapeutics, a company developing personalized T cell therapies targeting clonal neoantigens.

C.S. acknowledges grants from AstraZeneca, Boehringer-Ingelheim, Bristol Myers Squibb, Pfizer, Roche-Ventana, Invitae (previously Archer Dx Inc - collaboration in minimal residual disease sequencing technologies), Ono Pharmaceutical, and Personalis. He is Chief Investigator for the AZ MeRmaiD 1 and 2 clinical trials and is the Steering Committee Chair. He is also Co-Chief Investigator of the NHS Galleri trial funded by GRAIL and a paid member of GRAIL's Scientific Advisory Board. He receives consultant fees from Achilles Therapeutics (also SAB member), Bicycle Therapeutics (also an SAB member and Chair of the Clinical Advisory Group), Genentech, Medicxi, Novartis, China Innovation Centre of Roche (CICoR) formerly Roche Innovation Centre – Shanghai, Metabomed (until July 2022), Relay Therapeutics SAB member, Saga Diagnostics SAB member and the Sarah Cannon Research Institute. C.S. has received honoraria from Amgen, AstraZeneca, Bristol Myers Squibb, GlaxoSmithKline, Illumina, MSD, Novartis, Pfizer, and Roche-Ventana. C.S. has previously held stock options in Apogen Biotechnologies and GRAIL, and currently has stock options in Epic Bioscience, Bicycle Therapeutics, Relay Therapeutics, and has stock options and is co-founder of Achilles Therapeutics. C.S. declares a patent application for methods to detect lung cancer (PCT/US2017/028013); targeting neoantigens (PCT/EP2016/059401); identifying patient response to immune checkpoint blockade (PCT/EP2016/071471); methods for lung cancer detection (US20190106751A1); identifying patients who respond to cancer treatment (PCT/GB2018/051912); determining HLA LOH (PCT/GB2018/052004); predicting survival rates of patients with cancer (PCT/GB2020/050221); methods and systems for tumor monitoring (PCT/EP2022/077987); analysis of HLA alleles transcriptional deregulation (PCT/EP2023/059039). C.S. is an inventor on a European patent application (PCT/GB2017/053289) relating to assay technology to detect tumor recurrence. This patent has been licensed to a commercial entity and under their terms of employment C.S. is due a revenue share of any revenue generated from such license(s). C.S. is a Royal Society Napier Research Professor (RSRP\R\210001).

STAR★METHODS

Detailed methods are provided in the online version of this paper and include the following:

- KEY RESOURCES TABLE
- EXPERIMENTAL MODEL AND STUDY PARTICIPANT DETAILS
  - Human subjects
  - Processing of tumor and non-malignant lung tissue
  - Tumor organoid establishment and maintenance
  - TIL expansion
  - Model antigen T cells
  - Natural killer cells
- METHOD DETAILS
  - Isolation of pure tumor organoids
  - Generation of clonal organoid libraries
  - Immunohistochemistry and multiplex immunofluorescence
  - Organoid – T cell co-culture and T cell reactivity assays
  - NK cell reactivity assays
  - Cytometric bead array (CBA)
  - HLA class I and PD-L1 surface staining
  - NOA1 silencing
  - RT-qPCR
  - Lentivirus production
  - *CTAG1B* (NY-ESO-1) transduction of organoids
  - DNA sequencing
  - Genomic analysis
  - RNA sequencing
  - Differential gene expression analysis
  - Bulk T cell receptor beta chain (TCRb) sequencing
  - Single cell RNA and TCR sequencing
- QUANTIFICATION AND STATISTICAL ANALYSIS

SUPPLEMENTAL INFORMATION

Supplemental information can be found online at https://doi.org/10.1016/j.ccell.2025.06.012.

Received: June 15, 2024
Revised: March 31, 2025
Accepted: June 15, 2025

REFERENCES

1. Borghaei, H., Paz-Ares, L., Horn, L., Spigel, D.R., Steins, M., Ready, N.E., Chow, L.Q., Vokes, E.E., Felip, E., Holgado, E., et al. (2015). Nivolumab versus Docetaxel in Advanced Nonsquamous Non-Small-Cell Lung Cancer. N. Engl. J. Med. *373*, 1627–1639. https://doi.org/10.1056/NEJMoa1507643.
2. Gandhi, L., Rodríguez-Abreu, D., Gadgeel, S., Esteban, E., Felip, E., De Angelis, F., Domine, M., Clingan, P., Hochmair, M.J., Powell, S.F., et al. (2018). Pembrolizumab plus Chemotherapy in Metastatic Non-Small-Cell Lung Cancer. N. Engl. J. Med. *378*, 2078–2092. https://doi.org/10.1056/NEJMoa1801005.
3. Jia, Q., Wu, W., Wang, Y., Alexander, P.B., Sun, C., Gong, Z., Cheng, J.N., Sun, H., Guan, Y., Xia, X., et al. (2018). Local mutational diversity drives intratumoral immune heterogeneity in non-small cell lung cancer. Nat. Commun. *9*, 5361. https://doi.org/10.1038/s41467-018-07767-w.
4. Rosenthal, R., Cadieux, E.L., Salgado, R., Bakir, M.A., Moore, D.A., Hiley, C.T., Lund, T., Tanić, M., Reading, J.L., Joshi, K., et al. (2019). Neoantigen-directed immune escape in lung cancer evolution. Nature *567*, 479–485. https://doi.org/10.1038/s41586-019-1032-7.
5. Joshi, K., de Massy, M.R., Ismail, M., Reading, J.L., Uddin, I., Woolston, A., Hatipoglu, E., Oakes, T., Rosenthal, R., Peacock, T., et al. (2019). Spatial heterogeneity of the T cell receptor repertoire reflects the mutational landscape in lung cancer. Nat. Med. *25*, 1549–1559. https://doi.org/10.1038/s41591-019-0592-2.
6. AbdulJabbar, K., Raza, S.E.A., Rosenthal, R., Jamal-Hanjani, M., Veeriah, S., Akarca, A., Lund, T., Moore, D.A., Salgado, R., Al Bakir, M., et al. (2020). Geospatial immune variability illuminates differential evolution of lung adenocarcinoma. Nat. Med. *26*, 1054–1062. https://doi.org/10.1038/s41591-020-0900-x.
7. Xiao, Z., Todd, L., Huang, L., Noguera-Ortega, E., Lu, Z., Huang, L., Kopp, M., Li, Y., Pattada, N., Zhong, W., et al. (2023). Desmoplastic stroma restricts T cell extravasation and mediates immune exclusion and immunosuppression in solid tumors. Nat. Commun. *14*, 5110. https://doi.org/10.1038/s41467-023-40850-5.
8. Enfield, K.S.S., Colliver, E., Lee, C., Magness, A., Moore, D.A., Sivakumar, M., Grigoriadis, K., Pich, O., Karasaki, T., Hobson, P.S., et al. (2024). Spatial Architecture of Myeloid and T Cells Orchestrates Immune Evasion and Clinical Outcome in Lung Cancer. Cancer Discov. *14*, 1018–1047. https://doi.org/10.1158/2159-8290.CD-23-1380.
9. McGranahan, N., and Swanton, C. (2017). Clonal Heterogeneity and Tumor Evolution: Past, Present, and the Future. Cell *168*, 613–628. https://doi.org/10.1016/j.cell.2017.01.018.
10. Frankell, A.M., Dietzen, M., Al Bakir, M., Lim, E.L., Karasaki, T., Ward, S., Veeriah, S., Colliver, E., Huebner, A., Bunkum, A., et al. (2023). The evolution of lung cancer and impact of subclonal selection in TRACERx. Nature *616*, 525–533. https://doi.org/10.1038/s41586-023-05783-5.
11. Lakatos, E., Gunasri, V., Zapata, L., Househam, J., Heide, T., Trahearn, N., Swinyard, O., Cisneros, L., Lynn, C., Mossner, M., et al. (2024). Epigenome

and early selection determine the tumour-immune evolutionary trajectory of colorectal cancer. Preprint at bioRxiv. https://doi.org/10.1101/2024.02.12.579956.

12. Lomakin, A., Svedlund, J., Strell, C., Gataric, M., Shmatko, A., Rukhovich, G., Park, J.S., Ju, Y.S., Dentro, S., Kleshchevnikov, V., et al. (2022). Spatial genomics maps the structure, nature and evolution of cancer clones. Nature *611*, 594–602. https://doi.org/10.1038/s41586-022-05425-2.
13. Roerink, S.F., Sasaki, N., Lee-Six, H., Young, M.D., Alexandrov, L.B., Behjati, S., Mitchell, T.J., Grossmann, S., Lightfoot, H., Egan, D.A., et al. (2018). Intra-tumour diversification in colorectal cancer at the single-cell level. Nature *556*, 457–462. https://doi.org/10.1038/s41586-018-0024-3.
14. Dijkstra, K.K., Cattaneo, C.M., Weeber, F., Chalabi, M., van de Haar, J., Fanchi, L.F., Slagter, M., van der Velden, D.L., Kaing, S., Kelderman, S., et al. (2018). Generation of Tumor-Reactive T Cells by Co-culture of Peripheral Blood Lymphocytes and Tumor Organoids. Cell *174*, 1586–1598.e12. https://doi.org/10.1016/j.cell.2018.07.009.
15. Karasaki, T., Moore, D.A., Veeriah, S., Naceur-Lombardelli, C., Toncheva, A., Magno, N., Ward, S., Bakir, M.A., Watkins, T.B.K., Grigoriadis, K., et al. (2023). Evolutionary characterization of lung adenocarcinoma morphology in TRACERx. Nat. Med. *29*, 833–845. https://doi.org/10.1038/s41591-023-02230-w.
16. Dudley, M.E., Wunderlich, J.R., Shelton, T.E., Even, J., and Rosenberg, S.A. (2003). Generation of tumor-infiltrating lymphocyte cultures for use in adoptive transfer therapy for melanoma patients. J. Immunother. *26*, 332–342. https://doi.org/10.1097/00002371-200307000-00005.
17. Lowery, F.J., Krishna, S., Yossef, R., Parikh, N.B., Chatani, P.D., Zacharakis, N., Parkhurst, M.R., Levin, N., Sindiri, S., Sachs, A., et al. (2022). Molecular signatures of antitumor neoantigen-reactive T cells from metastatic human cancers. Science *375*, 877–884. https://doi.org/10.1126/science.abl5447.
18. Scheper, W., Kelderman, S., Fanchi, L.F., Linnemann, C., Bendle, G., de Rooij, M.A.J., Hirt, C., Mezzadra, R., Slagter, M., Dijkstra, K., et al. (2019). Low and variable tumor reactivity of the intratumoral TCR repertoire in human cancers. Nat. Med. *25*, 89–94. https://doi.org/10.1038/s41591-018-0266-5.
19. Simoni, Y., Becht, E., Fehlings, M., Loh, C.Y., Koo, S.L., Teng, K.W.W., Yeong, J.P.S., Nahar, R., Zhang, T., Kared, H., et al. (2018). Bystander CD8(+) T cells are abundant and phenotypically distinct in human tumour infiltrates. Nature *557*, 575–579. https://doi.org/10.1038/s41586-018-0130-2.
20. Sharma, P., Hu-Lieskovan, S., Wargo, J.A., and Ribas, A. (2017). Primary, Adaptive, and Acquired Resistance to Cancer Immunotherapy. Cell *168*, 707–723. https://doi.org/10.1016/j.cell.2017.01.017.
21. Gomez-Eerland, R., Nuijen, B., Heemskerk, B., van Rooij, N., van den Berg, J.H., Beijnen, J.H., Uckert, W., Kvistborg, P., Schumacher, T.N., Haanen, J.B.A.G., and Jorritsma, A. (2014). Manufacture of gene-modified human T-cells with a memory stem/central memory phenotype. Hum. Gene Ther. Methods *25*, 277–287. https://doi.org/10.1089/hgtb.2014.004.
22. Robbins, P.F., Li, Y.F., El-Gamil, M., Zhao, Y., Wargo, J.A., Zheng, Z., Xu, H., Morgan, R.A., Feldman, S.A., Johnson, L.A., et al. (2008). Single and dual amino acid substitutions in TCR CDRs can enhance antigen-specific T cell functions. J. Immunol. *180*, 6116–6131. https://doi.org/10.4049/jimmunol.180.9.6116.
23. Pons-Tostivint, E., Lugat, A., Fontenau, J.F., Denis, M.G., and Bennouna, J. (2021). STK11/LKB1 Modulation of the Immune Response in Lung Cancer: From Biology to Therapeutic Impact. Cells *10*, 3129. https://doi.org/10.3390/cells10113129.
24. van de Haar, J., Mankor, J.M., Hummelink, K., Monkhorst, K., Smit, E.F., Wessels, L.F.A., Cuppen, E., Aerts, J.G.J.V., and Voest, E.E. (2024). Combining Genomic Biomarkers to Guide Immunotherapy in Non-Small Cell Lung Cancer. Clin. Cancer Res. *30*, 1307–1318. https://doi.org/10.1158/1078-0432.CCR-23-4027.
25. Fei, L., Ren, X., Yu, H., and Zhan, Y. (2021). Targeting the CCL2/CCR2 Axis in Cancer Immunotherapy: One Stone, Three Birds? Front. Immunol. *12*, 771210. https://doi.org/10.3389/fimmu.2021.771210.
26. Batlle, E., and Massagué, J. (2019). Transforming Growth Factor-beta Signaling in Immunity and Cancer. Immunity *50*, 924–940. https://doi.org/10.1016/j.immuni.2019.03.024.
27. Lerner, E.C., Woroniecka, K.I., D'Anniballe, V.M., Wilkinson, D.S., Mohan, A.A., Lorrey, S.J., Waibl-Polania, J., Wachsmuth, L.P., Miggelbrink, A.M., Jackson, J.D., et al. (2023). CD8(+) T cells maintain killing of MHC-I-negative tumor cells through the NKG2D-NKG2DL axis. Nat. Cancer *4*, 1258–1272. https://doi.org/10.1038/s43018-023-00600-4.
28. Karre, K., Ljunggren, H.G., Piontek, G., and Kiessling, R. (1986). Selective rejection of H-2-deficient lymphoma variants suggests alternative immune defence strategy. Nature *319*, 675–678. https://doi.org/10.1038/319675a0.
29. Denisenko, E., de Kock, L., Tan, A., Beasley, A.B., Beilin, M., Jones, M.E., Hou, R., Muirí, D.Ó., Bilic, S., Mohan, G.R.K.A., et al. (2024). Spatial transcriptomics reveals discrete tumour microenvironments and autocrine loops within ovarian cancer subclones. Nat. Commun. *15*, 2860. https://doi.org/10.1038/s41467-024-47271-y.
30. McGranahan, N., Rosenthal, R., Hiley, C.T., Rowan, A.J., Watkins, T.B.K., Wilson, G.A., Birkbak, N.J., Veeriah, S., Van Loo, P., Herrero, J., et al. (2017). Allele-Specific HLA Loss and Immune Escape in Lung Cancer Evolution. Cell *171*, 1259–1271.e11. https://doi.org/10.1016/j.cell.2017.10.001.
31. Angelova, M., Mlecnik, B., Vasaturo, A., Bindea, G., Fredriksen, T., Lafontaine, L., Buttard, B., Morgand, E., Bruni, D., Jouret-Mourin, A., et al. (2018). Evolution of Metastases in Space and Time under Immune Selection. Cell *175*, 751–765.e16. https://doi.org/10.1016/j.cell.2018.09.018.
32. Al Bakir, M., Huebner, A., Martínez-Ruiz, C., Grigoriadis, K., Watkins, T.B.K., Pich, O., Moore, D.A., Veeriah, S., Ward, S., Laycock, J., et al. (2023). The evolution of non-small cell lung cancer metastases in TRACERx. Nature *616*, 534–542. https://doi.org/10.1038/s41586-023-05729-x.
33. de Vries, N.L., van de Haar, J., Veninga, V., Chalabi, M., Ijsselsteijn, M.E., van der Ploeg, M., van den Bulk, J., Ruano, D., van den Berg, J.G., Haanen, J.B., et al. (2023). gammadelta T cells are effectors of immunotherapy in cancers with HLA class I defects. Nature *613*, 743–750. https://doi.org/10.1038/s41586-022-05593-1.
34. Ramos Zapatero, M., Tong, A., Opzoomer, J.W., O'Sullivan, R., Cardoso Rodriguez, F., Sufi, J., Vlckova, P., Nattress, C., Qin, X., Claus, J., et al. (2023). Trellis tree-based analysis reveals stromal regulation of patient-derived organoid drug responses. Cell *186*, 5606–5619.e24. https://doi.org/10.1016/j.cell.2023.11.005.
35. Dijkstra, K.K., Monkhorst, K., Schipper, L.J., Hartemink, K.J., Smit, E.F., Kaing, S., de Groot, R., Wolkers, M.C., Clevers, H., Cuppen, E., and Voest, E.E. (2020). Challenges in Establishing Pure Lung Cancer Organoids Limit Their Utility for Personalized Medicine. Cell Rep. *31*, 107588. https://doi.org/10.1016/j.celrep.2020.107588.
36. Hughes, T., Dijkstra, K.K., Rawlins, E.L., and Hynds, R.E. (2022). Open questions in human lung organoid research. Front. Pharmacol. *13*, 1083017. https://doi.org/10.3389/fphar.2022.1083017.
37. Sachs, N., Papaspyropoulos, A., Zomer-van Ommen, D.D., Heo, I., Bottinger, L., Klay, D., Weeber, F., Huelsz-Prince, G., Iakobachvili, N., Amatngalim, G.D., et al. (2019). Long-term expanding human airway organoids for disease modeling. EMBO J. *38*, e100300. https://doi.org/10.15252/embj.2018100300.
38. Hynds, R.E., Huebner, A., Pearce, D.R., Hill, M.S., Akarca, A.U., Moore, D.A., Ward, S., Gowers, K.H.C., Karasaki, T., Al Bakir, M., et al. (2024). Representation of genomic intratumor heterogeneity in multi-region non-small cell lung cancer patient-derived xenograft models. Nat. Commun. *15*, 4653. https://doi.org/10.1038/s41467-024-47547-3.
39. Stewart, S.A., Dykxhoorn, D.M., Palliser, D., Mizuno, H., Yu, E.Y., An, D.S., Sabatini, D.M., Chen, I.S.Y., Hahn, W.C., Sharp, P.A., et al. (2003).

Lentivirus-delivered stable gene silencing by RNAi in primary cells. RNA *9*, 493–501. https://doi.org/10.1261/rna.2192803.

40. Grigoriadis, K., Huebner, A., Bunkum, A., Colliver, E., Frankell, A.M., Hill, M. S., Thol, K., Birkbak, N.J., Swanton, C., Zaccaria, S., and McGranahan, N. (2024). CONIPHER: a computational framework for scalable phylogenetic reconstruction with error correction. Nat. Protoc. *19*, 159–183. https://doi.org/10.1038/s41596-023-00913-9.
41. Waskom, M. (2021). seaborn: statistical data visualization. J. Open Source Softw. *6*, 3021. https://doi.org/10.2115/joss.03021.
42. Watkins, T.B.K., Colliver, E.C., Huska, M.R., Kaufmann, T.L., Lim, E.L., Duncan, C.B., Haase, K., Van Loo, P., Swanton, C., McGranahan, N., and Schwarz, R.F. (2023). Refphase: Multi-sample phasing reveals haplotype-specific copy number heterogeneity. PLoS Comput. Biol. *19*, e1011379. https://doi.org/10.1371/journal.pcbi.1011379.
43. Lex, A., Gehlenborg, N., Strobelt, H., Vuillemot, R., and Pfister, H. (2014). UpSet: Visualization of Intersecting Sets. IEEE Trans. Vis. Comput. Graph. *20*, 1983–1992. https://doi.org/10.1109/TVCG.2014.2346248.
44. Puttick, C., Jones, T.P., Leung, M.M., Galvez-Cancino, F., Liu, J., Varas-Godoy, M., Rowan, A., Pich, O., Martinez-Ruiz, C., Bentham, R., et al. (2024). MHC Hammer reveals genetic and non-genetic HLA disruption in cancer evolution. Nat. Genet. *56*, 2121–2131. https://doi.org/10.1038/s41588-024-01883-8.
45. Kawaguchi, S., Higasa, K., Shimizu, M., Yamada, R., and Matsuda, F. (2017). HLA-HD: An accurate HLA typing algorithm for next-generation sequencing data. Hum. Mutat. *38*, 788–797. https://doi.org/10.1002/humu.23230.
46. Reynisson, B., Alvarez, B., Paul, S., Peters, B., and Nielsen, M. (2020). NetMHCpan-4.1 and NetMHCIIpan-4.0: improved predictions of MHC antigen presentation by concurrent motif deconvolution and integration of MS MHC eluted ligand data. Nucleic Acids Res. *48*, W449–W454. https://doi.org/10.1093/nar/gkaa379.
47. Ritchie, M.E., Phipson, B., Wu, D., Hu, Y., Law, C.W., Shi, W., and Smyth, G.K. (2015). limma powers differential expression analyses for RNA-sequencing and microarray studies. Nucleic Acids Res. *43*, e47. https://doi.org/10.1093/nar/gkv007.
48. Love, M.I., Huber, W., and Anders, S. (2014). Moderated estimation of fold change and dispersion for RNA-seq data with DESeq2. Genome Biol. *15*, 550. https://doi.org/10.1186/s13059-014-0550-8.
49. Robinson, M.D., McCarthy, D.J., and Smyth, G.K. (2010). edgeR: a Bioconductor package for differential expression analysis of digital gene expression data. Bioinformatics *26*, 139–140. https://doi.org/10.1093/bioinformatics/btp616.
50. Korotkevich, G., Sukhov, V., Budin, N., Shpak, B., Artyomov, M.N., and Sergushichev, A. (2021). Fast gene set enrichment analysis. Preprint at bioRxiv. https://doi.org/10.1101/060012.
51. Thomas, N., Heather, J., Ndifon, W., Shawe-Taylor, J., and Chain, B. (2013). Decombinator: a tool for fast, efficient gene assignment in T-cell receptor sequences using a finite state machine. Bioinformatics *29*, 542–550. https://doi.org/10.1093/bioinformatics/btt004.
52. Wolf, F.A., Angerer, P., and Theis, F.J. (2018). SCANPY: large-scale single-cell gene expression data analysis. Genome Biol. *19*, 15. https://doi.org/10.1186/s13059-017-1382-0.
53. Rueden, C.T., Schindelin, J., Hiner, M.C., DeZonia, B.E., Walter, A.E., Arena, E.T., and Eliceiri, K.W. (2017). ImageJ2: ImageJ for the next generation of scientific image data. BMC Bioinf. *18*, 529. https://doi.org/10.1186/s12859-017-1934-z.
54. Cattaneo, C.M., Dijkstra, K.K., Fanchi, L.F., Kelderman, S., Kaing, S., van Rooij, N., van den Brink, S., Schumacher, T.N., and Voest, E.E. (2020). Tumor organoid-T-cell coculture systems. Nat. Protoc. *15*, 15–39. https://doi.org/10.1038/s41596-019-0232-9.
55. Kim, M., Mun, H., Sung, C.O., Cho, E.J., Jeon, H.J., Chun, S.M., Jung, D.J., Shin, T.H., Jeong, G.S., Kim, D.K., et al. (2019). Patient-derived lung cancer organoids as in vitro cancer models for therapeutic screening. Nat. Commun. *10*, 3991. https://doi.org/10.1038/s41467-019-11867-6.
56. Liberzon, A., Birger, C., Thorvaldsdóttir, H., Ghandi, M., Mesirov, J.P., and Tamayo, P. (2015). The Molecular Signatures Database (MSigDB) hallmark gene set collection. Cell Syst. *1*, 417–425. https://doi.org/10.1016/j.cels.2015.12.004.
57. Subramanian, A., Tamayo, P., Mootha, V.K., Mukherjee, S., Ebert, B.L., Gillette, M.A., Paulovich, A., Pomeroy, S.L., Golub, T.R., Lander, E.S., and Mesirov, J.P. (2005). Gene set enrichment analysis: a knowledge-based approach for interpreting genome-wide expression profiles. Proc. Natl. Acad. Sci. USA *102*, 15545–15550. https://doi.org/10.1073/pnas.0506580102.
58. Oakes, T., Heather, J.M., Best, K., Byng-Maddick, R., Husovsky, C., Ismail, M., Joshi, K., Maxwell, G., Noursadeghi, M., Riddell, N., et al. (2017). Quantitative Characterization of the T Cell Receptor Repertoire of Naive and Memory Subsets Using an Integrated Experimental and Computational Pipeline Which Is Robust, Economical, and Versatile. Front. Immunol. *8*, 1267. https://doi.org/10.3389/fimmu.2017.01267.
59. Miller, B.C., Sen, D.R., Al Abosy, R., Bi, K., Virkud, Y.V., LaFleur, M.W., Yates, K.B., Lako, A., Felt, K., Naik, G.S., et al. (2019). Subsets of exhausted CD8(+) T cells differentially mediate tumor control and respond to checkpoint blockade. Nat. Immunol. *20*, 326–336. https://doi.org/10.1038/s41590-019-0312-6.
60. Guo, X., Zhang, Y., Zheng, L., Zheng, C., Song, J., Zhang, Q., Kang, B., Liu, Z., Jin, L., Xing, R., et al. (2018). Global characterization of T cells in non-small-cell lung cancer by single-cell sequencing. Nat. Med. *24*, 978–985. https://doi.org/10.1038/s41591-018-0045-3.
61. Ng, P.C., and Henikoff, S. (2003). SIFT: Predicting amino acid changes that affect protein function. Nucleic Acids Res. *31*, 3812–3814. https://doi.org/10.1093/nar/gkg509.
62. Adzhubei, I.A., Schmidt, S., Peshkin, L., Ramensky, V.E., Gerasimova, A., Bork, P., Kondrashov, A.S., and Sunyaev, S.R. (2010). A method and server for predicting damaging missense mutations. Nat. Methods *7*, 248–249. https://doi.org/10.1038/nmeth0410-248.

Please cite this article in press as: Dijkstra et al., Subclonal immune evasion in non-small cell lung cancer, Cancer Cell (2025), https://doi.org/10.1016/j.ccell.2025.06.012

STAR★METHODS

KEY RESOURCES TABLE

REAGENT or RESOURCE	SOURCE	IDENTIFIER
Antibodies		
Ultra-LEAF purified mouse anti-human CD274	BioLegend	29E.2A3; Cat# 329715; RRID:AB_11149486
Mouse anti-human CD3	eBioscience	OKT-3; Cat#16-0037-85; RRID:AB_468855
Rabbit anti-human CK5	Abcam	EP1601Y; Cat# ab52635; RRID:AB_869890
DISCOVERY OmniMAP anti-rabbit HRP	Roche	Roche Cat# 760–4311; RRID:AB_2811043
Mouse anti-human cytokeratin	Agilent	AE1/AE3; Cat# M3515; RRID:AB_2132885
Anti-myeloperoxidase (MPO) antibody	Abcam	EPR20257; Cat# ab208670, RRID:AB_2864724
Mouse anti-human CD68	Agilent	KP1; Cat# GA60961-2; RRID:AB_2661840
Mouse anti-human FOXP3	Abcam	236A/E7; Cat# ab20034, RRID:AB_445284
Mouse anti-human CD8	Agilent	C8/144B; Cat# GA623; RRID:AB_3073940
Rabbit anti-human CD3G	Abcam	EPR4517; Cat# ab134096
Mouse anti-human smooth muscle actin (SMA)	Agilent	1A4; Cat# M0851; RRID:AB_2223500
Anti-NCAM1 antibody	Abcam	CAL53; Cat# ab237708; RRID:AB_3676336
Mouse anti-human CD3 (BB700 conjugated)	Becton Dickinson (BD) Biosciences	SK7; Cat# 566575; RRID:AB_2860004
Mouse anti-human CD4 (FITC conjugated)	BD Biosciences	RPA-T4; Cat#555346; RRID:AB_395751
Mouse anti-human CD8 (BV421 conjugated)	BD Biosciences	RPA-T8; Cat# 562428; RRID:AB_11154035
Mouse anti-human CD137 (PE conjugated)	BD Biosciences	4B4-1; Cat#550890; RRID:AB_398477
Mouse anti-human HLA-A2 (APC conjugated)	Thermo Fisher Scientific (eBioscience)	BB7.2; Cat# 17-9876-41; RRID:AB_11151522
Mouse anti-human HLA-ABC (PE conjugated)	BD Biosciences	Cat# 560964; RRID:AB_10563764
Mouse anti-human PD-L1 (APC conjugated)	Thermo Fisher Scientific (eBioscience)	MIH1; Cat# 17-5983-41; RRID:AB_10597280
Ultra-LEAF purified anti-human MICA/MICB	BioLegend	6D4; Cat# 320919; RRID:AB_2814175
Ultra-LEAF purified mouse IgG2a, kappa isotype control	BioLegend	MOPC-173; Cat# 400264; RRID:AB_11148947
MHC-I blocking antibody	The Francis Crick Institute	Clone W6/32 from hybridoma ATCC HB95
Mouse anti-human CD16 (AF700 conjugated)	BioLegend	3G6; Cat# 302025; RRID:AB_2278418
Mouse anti-human CD56 (NCAM) (BV605 conjugated)	BioLegend	5.1H11; Cat# 362537; RRID:AB_2565855
Mouse IgG1 kappa isotype control (APC conjugated)	Thermo Fisher Scientific (eBioscience)	P3.6.2.8.1; Cat# 17-4714-42; RRID:AB_1603315
Mouse IgG1 kappa isotype control (PE conjugated)	BD Biosciences	MOPC-21; Cat# 556650; RRID:AB_396514
Bacterial and virus strains		
pLVX-CMV-CTAG1B (NY-ESO1)-IRES-ZsGreen	This paper	N/A
pLVX-CMV-Stuffer-IRES-ZsGreen_empty	This paper	N/A
Biological samples		
Non-small cell lung cancer resection specimens	This study	N/A
Tumor-infiltrating lymphocytes (TIL)	This study	N/A
Patient-derived xenograft (PDX)	Hynds et al.[38]	CRUK0718
Human peripheral blood buffy coat	Tebu-Bio	297CTIPB.1.24-fresh
Human peripheral blood buffy coat	Sanquin, the Netherlands	B2825R00
Chemicals, peptides, and recombinant proteins		
B27 supplement	GIBCO	Cat#17504-044
N-Acetylcysteine	Sigma-Aldrich	Cat#A9165-5G
Nicotinamide	Sigma-Aldrich	Cat#N0636
Human recombinant EGF	Peprotech	Cat#AF-100-15

(*Continued on next page*)

Please cite this article in press as: Dijkstra et al., Subclonal immune evasion in non-small cell lung cancer, Cancer Cell (2025), https://doi.org/10.1016/j.ccell.2025.06.012

CellPress
OPEN ACCESS

Continued

REAGENT or RESOURCE	SOURCE	IDENTIFIER
A83-01	Tocris	Cat#2939
SB202190	Cayman Chemicals	Cat#10010399
Y-27632	Selleckchem	Cat#S1049
Human recombinant FGF-2	Peprotech	Cat#100-18B
Human recombinant FGF-7	Peprotech	Cat#100-19
Human recombinant FGF-10	Peprotech	Cat#100-26
Geltrex LDEV-free reduced growth factor basement membrane	GIBCO	Cat#A1413202
Cultrex reduced growth factor basement membrane extract, type 2, Select	BioTechne	Cat#3536-001-02
Collagenase type I	Gibco	Cat#17-100-017
Collagenase type II	Sigma-Aldrich	Cat#C6885
DNAse I	Roche	Cat#4716728001
DMEM-F12	GIBCO	Cat#31331-028
Advanced DMEM-F12	GIBCO	Cat#12634-028
Opti-MEM	Gibco	Cat#31985-062
TexMacs medium	Miltenyi	Cat#130-097-196
Penicillin/streptomycin	GIBCO	Cat#15070063
Ultraglutamine type I	Lonza	Cat#BE17-605E
HEPES	GIBCO	Cat#15630-056
Accutase	GIBCO	Cat#A1110501
Recovery Cell Culture Freezing Medium	GIBCO	Cat#12648-010
RPMI 1640	GIBCO	Cat#11875093
Human serum, from human male AB plasma	Sigma-Aldrich	Cat#H3667
Benzonase	Merck	Cat#70746-3
Human recombinant interferon gamma	Peprotech	Cat#300-02
Phorbol 12-myristate 13-acetate (PMA)	Sigma-Aldrich	Cat#19-144
Ionomycin	Sigma-Aldrich	Cat#I9657
Dispase type II	Sigma-Aldrich	Cat#D4693
Interleukin-2	Slotervaart Medical Center	Proleukin
Ficoll-Paque Plus	GE Healthcare	Cat#17-1440-02
Recombinant human IL-21	Peprotech	Cat#AF-200-21
Recombinant human IL-15	Peprotec	Cat#AF-200-15
Lympholyte	CedarLane	Cat#CL5020
UltraPlast premium embedding medium	Solmedia	Cat#WAX060-T
Epitope retrieval solution 1	Leica	Cat#AR9961
Epitope retrieval solution 2	Leica	Cat#AR9640
DAPI	Thermo Fisher Scientific	Cat#62248
Prolong Gold Antifade reagent	Invitrogen	Cat#36934
Near-IR fixable viability dye	Invitrogen	Cat#L34994
NY-ESO-1 peptide (SLLMWITQC)	PepScan	N/A
MART-1 peptide (ELAGIGILTV)	ProteoGenix	N/A
Lipofectamine RNAiMAX Transfection reagent	ThermoFisher	Cat#13778100
Polyethylenimine (PEI)	Polysciences	Cat#23966
Polybrene	Merck Millipore	Cat#TR-1003-G
Primocin	Invivogen	Cat#ant-pm-1
Critical commercial assays		
Tumor cell dissociation kit, human	Miltenyi	Cat#130-095-929
$CD8^+$ T cell isolation kit, human	Miltenyi	Cat#130-096-495

(*Continued on next page*)

Continued

REAGENT or RESOURCE	SOURCE	IDENTIFIER
NK cell isolation kit, human	Miltenyi	Cat#130-092-657
Discovery ChromoMap DAB kit	Roche	Cat#760-159
Novolink polymer detection system	Leica	Cat#RE7260-CE
Cytometric bead array (CBA) human IFNg flex set	BD Biosciences	Cat#558269
AllPrep DNA/RNA isolation kit	Qiagen	Cat#80204
RNEasy isolation kit	Qiagen	Cat#74104
High-Capacity complementary DNA Reverse Transcription Kit	ThermoFisher	Cat#4368814
Fast SYBR green master mix	ThermoFisher	Cat#4385610
Maxima First Strand cDNA synthesis kit	ThermoFisher	Cat#K1671
SensiFAST SYBR Hi-ROX kit	Meridian Bioscience	Cat#92005
KAPA mRNA HyperPrep kit	Roche	Cat#08098115702
Human Core Exome kit	Twist Bioscience	Cat#PN100254
NEBNext® Ultra™ II DNA Library Prep Kit for Illumina	New England Biolabs	Cat#E7645L/E7103L
Human core exome panel	Twist Bioscience	Cat#100254
Twist Universal Blockers	Twist Bioscience	Cat#100578
Twist Fast Hybridisation Reagents	Twist Bioscience	Cat#100964
Twist Fast Wash Buffers	Twist Bioscience	Cat#100971
Chromium Next GEM Single-cell 5′ kit v2	10x Genomics	Cat#PN-1000263
Deposited data		
Processed sequencing data	This paper	https://doi.org/10.5281/zenodo.11520198
Raw sequencing data	This paper	EGA; dataset accession code EGAD00001015537
Experimental models: Cell lines		
R-spondin producer cell line	Laboratory of Calvin Kuo, Stanford, USA	293T-HA-RspoI-Fc
Noggin producer cell line	Laboratory of Hans Clevers, Utrecht, the Netherlands	HEK293-mNoggin-Fc
Human normal airway and non-small cell lung cancer organoids	This paper	N/A
NY-ESO-1 T cells	Laboratory of Martin Pule, London, UK	N/A
MART-1 T cells	Laboratory of John Haanen, Amsterdam, the Netherlands	N/A
Oligonucleotides		
NOA1 Silencer siRNA (ID: 147930)	ThermoFisher	Cat#AM16708
Silencer negative control No. 1 siRNA	ThermoFisher	Cat#AM4611
CTAG1B FWD primer (GCTTGAGTTCTACCTCGCCA)	IDT	N/A
CTAG1B REV primer (ATGTTGCCGGACACAGTGAA)	IDT	N/A
HPRT FWD primer (AGCCAGACTTTGTTGGATTTG)	IDT	N/A
HPRT REV primer (TTTACTGGCGATGTCAATAAG)	IDT	N/A
TBP FWD primer (CGGCTGTTTAACTTCGCTTC)	IDT	N/A
TBP REV primer (CACACGCCAAGAAACAGTGA)	IDT	N/A
UBC FWD primer (ATTTGGGTCGCGGTTCTTG)	IDT	N/A
UBC REV primer (TGCCTTGACATTCTCGATGGT)	IDT	N/A
NOA1 FWD primer (CCTGCAGGGAAATCAGTCAG)	IDT	N/A
NOA1 REV primer (TCCACCCATTGGAATCTGGA)	IDT	N/A
GADPH FWD primer (TTAAAAGCAGCCCTGGTGAC)	IDT	N/A
GAPDH REV primer (CTCTGCTCCTCCTGTTCGAC)	IDT	N/A

(*Continued on next page*)

Please cite this article in press as: Dijkstra et al., Subclonal immune evasion in non-small cell lung cancer, Cancer Cell (2025), https://doi.org/10.1016/j.ccell.2025.06.012

CellPress
OPEN ACCESS

Continued

REAGENT or RESOURCE	SOURCE	IDENTIFIER
Recombinant DNA		
pCMV-ΔR8.2-dvpr plasmid DNA	Stewart et al.[39]	Addgene, Cat#8455
pCMV VSV-G plasmid DNA	Stewart et al.[39]	Addgene, Cat#8454
pLVX-CMV-CTAG1B (NY-ESO1)-IRES-ZsGreen plasmid DNA	Laboratory of Manuel Varas, San Sebastian University, Chile	N/A
pLVX-CMV-Stuffer-IRES-ZsGreen_ empty plasmid DNA	Laboratory of Manuel Varas, San Sebastian University, Chile	N/A
Software and algorithms		
R (v4.2.2)	R Core Team	www.r-project.org
Prism (v10.0.3)	GraphPad	www.graphpad.com
Python (v3.8)	Python Software Foundation	www.python.org
Exome sequencing processing pipeline	Frankell et al.[10]	N/A
Conpiher (v2.1.0)	Grigoriadis et al.[40]	https://github.com/McGranahanLab/CONIPHER
seaborn.clustermap (v0.12.2)	Waskom[41]	https://seaborn.pydata.org/generated/seaborn.clustermap.html
Refphase (v0.3.2)	Watkins et al.[42]	https://bitbucket.org/schwarzlab/refphase/src/master/
Upsetplot (v0.8.0)	Lex et al.[43]	https://upsetplot.readthedocs.io/en/stable/
MHC Hammer	Puttick et al.[44]	https://github.com/McGranahanLab/mhc-hammer
HLA-HD (v1.2.1)	Kawaguchi et al.[45]	https://w3.genome.med.kyoto-u.ac.jp/HLA-HD/
NetMCHpan4.1	Reynisson et al.[46]	https://services.healthtech.dtu.dk/services/NetMHCpan-4.1/
Limma-voom (v.3.54.1)	Ritchie et al.[47]	https://bioconductor.org/packages/release/bioc/html/limma.html
DESeq2 (v.1.38.3)	Love et al.[48]	https://bioconductor.org/packages/release/bioc/html/DESeq2.html
edgeR (v.3.40.2)	Robinson et al.[49]	https://bioconductor.org/packages/release/bioc/html/edgeR.html
fgsea (v1.16.0)	Korotkevich et al.[50]	https://bioconductor.org/packages/release/bioc/html/fgsea.html
msigdbr (v7.5.1)	Dolgalev	https://igordot.github.io/msigdbr/
Decombinator	Thomas et al.[51]	https://github.com/innate2adaptive/Decombinator
ImmunoSeq Analyzer	Adaptive Biotechnologies	https://clients.adaptivebiotech.com
Cell Ranger (v6.0)	10x Genomics	https://support.10xgenomics.com/single-cell-gene-expression/software/pipelines/latest/what-is-cell-ranger
Scanpy (v1.9.1)	Wolf et al.[52]	https://scanpy.readthedocs.io/
ImageJ (v2.1.0)	Rueden et al.[53]	https://imagej.net/ij/

EXPERIMENTAL MODEL AND STUDY PARTICIPANT DETAILS

Human subjects

Patients were recruited in the Tracking Cancer Evolution through Therapy (TRACERx) clinical study, which was approved by an independent research ethics committee (13/LO/1546; https://clinicaltrials.gov/ct2/show/NCT01888601). Written informed consent was obtained from each patient. Patient 2 is part of the recently published TRACERx 421 cohort[10] and PDX established from this patient's tumor have been described recently.[38] Patients are known under study identifiers CRUK1398 (patient 1; male), CRUK0718 (patient 2; male), and CRUK1378 (patient 3; female).

Processing of tumor and non-malignant lung tissue

Tumor and non-malignant lung tissue was obtained from patients undergoing surgical resection of a primary NSCLC. Tissue was immediately transported on ice from the operation theater to a pathology laboratory, where the tumor was sampled at multiple different, spatially separated regions by a pathologist. In one case (patient 2), regional tissue samples were first expanded as PDX[38] prior to organoid establishment. In other cases, organoids were established directly from fresh tumor tissue. Tumor and non-malignant lung tissue was collected in Ad-DF+++ medium (Advanced DMEM/F12 (Gibco) supplemented with 2 mM Ultraglutamine I (Lonza), 10 mM HEPES (Gibco), and 100 U/mL pencillin / 100 μg/mL streptomycin (Gibco)), further supplemented with 1x Primocin (Invivogen) and stored on ice. Samples were processed for organoid establishment within 24 h after resection.

All plasticware was first coated by rinsing with a 1% fetal calf serum (FCS)/PBS solution to prevent sticking of tumor cells or fragments to plastics. Tumor samples were washed in phosphate buffer saline (PBS), dissected into small fragments using surgical scalpels and resuspended into 2.3 mL digestion buffer (Tumor Dissociation Kit, Miltenyi). Tumors were digested following manufacturer's instructions for 60 min on a gentleMACS system. Digested tumor fragments were passed through a 70 μm strainer and pelleted by centrifugation (300 g, 4′, room temperature). If the cell pellet was red, cells were incubated for 5 min in red blood cell lysis buffer (8.26 g/L ammonium chloride, 1 g/L sodium bicarbonate, 0.1 mM EDTA in distilled water) at room temperature. Cells were washed twice with PBS and pelleted by centrifugation.

Non-malignant lung tissue was dissected into small fragments and resuspended in 10 mL lung digestion buffer (1.5 mg/mL collagenase type II (Sigma-Aldrich), 500 μg/mL dispase type II (Sigma-Aldrich), 10 μM Y-27632 (Selleck Chemicals) and 1:500 Primocin in PBS). Cells were incubated for 30–60 min at 37°C and mixed every 10–15 min by resuspension with 10 mL stripettes. Digestion was terminated after 60 min, or when tissue had largely dissociated into small clusters or single cells. Cells were pelleted by centrifugation (300 g, 4′, room temperature). If the cell pellet was red, cells were incubated for 5 min in red blood cell lysis buffer at room temperature. Cells were washed three times with PBS and pelleted by centrifugation.

Tumor or normal lung cells were either seeded for organoid culture (see below) or frozen in ice-cold 10% dimethyl sulfoxide (DMSO)/FCS or Recovery Cell Culture Freezing medium (Gibco) in a freezing container at −80°C and transferred to liquid nitrogen the next day.

Tumor organoid establishment and maintenance

Establishment of tumor and normal airway organoids was performed using previously published methods,[54] with some adaptations. Briefly, tumor cells from processed tissue were resuspended in ice-cold basement membrane extract (BME; Geltrex LDEV-free reduced growth factor basement membrane matrix (Gibco) or Cultrex reduced growth factor basement membrane extract, type 2, Select (BioTechne)), diluted 2:1 with DMEM-F12+ (DMEM-F12 supplemented with 100 U/mL pencillin / 100 μg/mL streptomycin). After solidification of BME (20′ at 37°C), tumor organoids from patients 1 and 2 were overlaid with minimal basic medium (MBM) to prevent outgrowth of normal airway organoids.[55] Tumor organoids from patient 3 did not grow in MBM and were cultured in complete lung organoid medium instead,[37] as were normal airway organoids. MBM consists of DMEM/F12+, supplemented with 1x B27 supplement (Gibco), 1x *N*-2 supplement (Gibco), 50 ng/mL human recombinant EGF (Peprotech), 20 ng/mL human recombinant FGF-2 (Peprotech) and 10 μM Y-27632 (Selleckchem). Complete lung medium consists of Advanced DMEM/F12 (Gibco), supplemented with 100 U/mL pencillin / 100 μg/mL streptomycin, 2 mM Ultraglutamine I (Lonza), 10 mM HEPES (Gibco), 10% Noggin-conditioned medium, 10% R-spondin-1-conditioned medium, 1x B27 supplement (Gibco), 10 mM nicotinamide (Sigma-Aldrich), 1.25 mM N-Acetylcysteine (Sigma-Aldrich), 500 nM A83-01 (Tocris Bioscience), 1 μM SB202190 (Cayman Chemicals), 25 ng/mL FGF-7 (Peprotech), 100 ng/mL FGF-10 (Peprotech), and 5 μM Y-27632 (Selleckchem). R-spondin1-conditioned medium was produced from 293T-HA-RspoI-Fc producer cell lines (obtained from C. Kuo, Stanford) and Noggin-conditioned medium from HEK293-mNoggin-Fc cell lines (obtained from J. den Hertog, Utrecht). Organoids were passaged by isolating organoids from BME by washing with cold PBS, followed by dissociation with accutase (Gibco) for 3–10′ at 37°C. Single cells or small cell clusters were re-seeded in BME and cultured as above. Master and working biobanks were cryopreserved as previously described.[54] Organoids were authenticated using short tandem repeat (STR) profiling and regularly tested for contamination with Mycoplasma.

TIL expansion

Fresh tumor and normal adjacent tissue were cut into ~1–2 mm^3 pieces and enzymatically digested in 3 mL RPMI-1640 (Sigma) with 34.4 μg/mL Collagenase Type I (Gibco) and 75 μg/mL DNase I (Roche), followed by mechanical disaggregation using a gentleMACS Octo Dissociator (Miltenyi Biotec) at 37°C for 1 h with constant slow mixing. A single cell suspension was obtained by filtering the digest over a 70 μm strainer with 5 mL complete RPMI-1640 supplemented with 2% fetal bovine serum (FBS; Gibco or PAN Biotech), 1% L-glutamine (Sigma), and 100 U/mL pencillin / 100 μg/mL streptomycin. TIL were subsequently isolated by density gradient centrifugation (750 g, 10 min) on Ficoll-Paque Plus (GE Healthcare). The buffy coat was collected at the interface, washed twice in complete RPMI, resuspended in 90% FBS with 10% DMSO (Sigma) and cryopreserved prior to downstream analysis.

Cryopreserved TIL were expanded in two phases in an adaptation to our previous protocol for expansion of peripheral blood lymphocytes.[14,54] In a pre-rapid expansion protocol (pre-REP), thawed TIL were resuspended in TexMACS medium (Miltenyi) supplemented with 5% human serum (Sigma-Aldrich) and 100/100 U/mL penicillin/streptomycin. TIL were combined with mixtures of all autologous regional organoids for that patient that were stimulated with 20 ng/mL IFNg (Peprotech) for 24 h prior to co-culture, at a 5:1 T cell:tumor cell ratio. Co-cultures were performed in the presence of 6000 U/mL IL-2 (Proleukin), 25 ng/mL IL-21 (Peprotech),

10 μg/mL Ultra-LEAF purified anti-CD274 antibody (Clone 29E.2A3, Biolegend), and 1:500 Primocin. TIL were expanded for 3 weeks in a pre-REP with weekly restimulation with fresh organoids.

After pre-REP, TIL were further expanded in 1–2 cycles of a REP,[16] by stimulation with 30 ng/mL anti-CD3 (OKT-3, eBioscience), 3000 U/mL IL-2, and 1:100 40 Gy irradiated feeder cells from three pooled healthy donors (Tebu-Bio). After two weeks of REP, cells were rested for 1 week in T cell medium (RPMI 1640 medium (Gibco) supplemented with 10% human serum and 100/100 U/mL penicillin/streptomycin) with 100 U/mL IL-2 before cryopreservation.

Model antigen T cells

NY-ESO-1 T cells were kindly provided by Angeliki Karamani, Manar Shafat, Gordon Weung-Kit Cheung and Martin Pule, purified for $CD8^+$ T cells using a $CD8^+$ T cell isolation kit (Miltenyi) and expanded in a REP as described above for TIL. MART-1 specific T cells were kindly provided by Ton Schumacher, John Haanen and Wouter Scheper. MART-1 and NY-ESO-1 T cells were maintained in T cell medium with 100 U/mL IL-2.

Natural killer cells

Peripheral blood mononuclear cells (PBMC) were isolated from buffy coats obtained from healthy anonymous donors (Sanquin, Amsterdam, the Netherlands) using Lympholyte (Cedarlane) density gradient separation. Thereafter, NK cells were isolated using a human NK cell isolation kit (Miltenyi) according to manufacturer's instructions and cryopreserved until further use. Two days before co-culture with organoids, NK cells were thawed and cultured with 10 ng/mL IL15 (Peprotech) at a concentration of $1–2*10^6$ cells in T cell medium.

METHOD DETAILS

Isolation of pure tumor organoids

Initial cultures from patient 3 contained a mixture of tumor and normal organoids (Figure S1B).[35] Tumor organoids were more cystic than normal airway organoids and readily dissociated upon repeated resuspension. Pure tumor organoid cultures were generated by passing dissociated organoids through a 100 μm strainer, which only passed through dissociated tumor organoids and retained undissociated normal airway organoids.

Generation of clonal organoid libraries

Regional organoids were passaged to single cells using accutase and re-seeded sparsely in BME. Single cells were allowed to grow out into large individual organoids. Single organoids were individually isolated by manual removal using a P200 pipette tip and transferred to a pre-coated (1% FCS/PBS) Eppendorf tube. Tubes containing single organoids were centrifuged (300 g, 4′) and as much supernatant was removed as possible without disturbing the organoid. Single organoids were resuspended in diluted BME and seeded into 96-well plates and cultured as described above.

Immunohistochemistry and multiplex immunofluorescence

Organoids were isolated from BME by washing with ice-cold PBS and fixed in neutral buffer formalin (NBF) for 1 h at room temperature. For cystic organoids, to preserve their integrity, media was removed from organoid cultures and organoids were directly resuspended in NBF for 24 h without centrifugation. After fixation, NBF was removed and organoids were embedded in 2–4% agarose. Organoids were standardly processed on a Tissue Tek VIP 6 tissue processor, embedded in UltraPlast Premium Embedding Medium (Solmedia Wax 060-T) and sectioned on a Leica RM microtome at 3 μm. The slides were the loaded onto a Tissue Tek Prima autostainer for staining on the routine Haematoxylin and Eosin protocol. The CK5 (Abcam AB52635) IHC was performed on the Roche Discovery Ultra Ventana platform, using an antibody dilution of 1:2000, antigen retrieval with CC1 for 48 min and primary antibody incubation for 60 min, followed by Roche Omnimap anti-rabbit HRP, before Chromomap DAB application (Roche).

For multiplex immunofluorescence (IF) of FFPE slides, tissue was fixed for 24h in 10% NBF before processing to wax using a Tissue-Tek VIP 6 AI processor. 3 μm FFPE sections were cut and baked for 1h at 60°C before staining was performed on the Leica Bond Rx platform. Hydrogen peroxide (3%) was used to block the endogenous peroxidase and 0.1% BSA solution was used for protein blocking. Antigen retrieval stripping steps between each antibody were performed with either Epitope Retrieval Solution 1 or Epitope Retrieval Solution 2 (Leica) for 20 min. Three triple IF stainings were performed and antibodies were applied with Opal pairings in the following order: Panel 1 – PanCK (Agilent, M3515) 1:200 with Opal 520 1:500, MPO (abcam, ab208670) 1:2000 with Opal 570 1:500, and CD68 (Agilent, GA60961-2) RTU with Opal 690 1:200. Panel 2 – FoxP3 (abcam, ab20034) 1:100 with Opal 570 1:500, CD8 (Agilent, GA623) RTU with Opal 690 1:200, and CD3 (abcam, ab134096) 1:500 with Opal 520 1:500. Panel 3: aSMA (Agilent, M0851) 1:250 with Opal 570 1:500, CD8 (Dako, GA623) RTU with Opal 690 1:200, and NCAM1/CD56 (abcam, ab237708) 1:2000 with Opal 520 1:500. Bond rabbit anti-mouse and mouse HRP anti-rabbit Polymer (Leica) was used as secondary detection. Slides were counterstained with DAPI (Thermo Scientific) 1:2500. Slides were mounted with Prolong Gold Antifade reagent (Invitrogen, P36934). Stained samples were acquired using an Olympus Slideview VS220 automated slide scanner. Fluorescence images were taken using a 20x/0.8 UPLXAPO objective and Brightline Sedat Pentaband filterset from Semrock (DA/FI/TR/Cy5/Cy7-5X5M-B-000) to acquire the respective channels. Image processing, including background subtraction and visualisation, was performed with python v3.8.17 (package skimage) and ImageJ v2.1.0 (IJ2 linux64 launcher).[53]

Please cite this article in press as: Dijkstra et al., Subclonal immune evasion in non-small cell lung cancer, Cancer Cell (2025), https://doi.org/10.1016/j.ccell.2025.06.012

Organoid – T cell co-culture and T cell reactivity assays

Organoids were dissociated to single cells using accutase and passed through a 40 μm strainer. Expanded TILs were thawed 1–3 days prior to co-culture and maintained in T cell medium with 100 U/mL IL-2. TIL were combined with dissociated tumor cells at a 2:1 ratio in T cell medium and plated at 0.5–1*10^5 T cells/well in a U-bottom 96-well plate. Reactivity assays were performed in the presence (reactivity of TIL against regional and clonal organoids) or absence (assays comparing reactivity to normal and tumor organoids; NY-ESO-1 and MART-1 T cell assays) of 100 U/mL IL-2. Phorbol myristate acetate (PMA; 50 ng/mL) and ionomycin (1 μg/mL) served as positive control. After 20–24 h of co-culture, 100 μL supernatant was collected for cytokine analysis (see below), and cells were washed twice in flow cytometry buffer (PBS supplemented with 0.1% bovine serum albumin (BSA) and 2.5 mM ethylenediamine tetraacetic acid (EDTA)) and stained with the following antibodies (all Becton Dickinson (BD) Biosciences) in flow cytometry buffer for 30′ at 4°C: anti-CD3-BB700 (SK7; 1:200 dilution), anti-CD4-FITC (RPA-T4; 1:20), anti-CD8-BV421 (RPA-T8; 1:200), anti-CD137-PE (4B4-1; 1:30), and live/dead fixable near-IR dead cell dye (Invitrogen; 1:200). Cells were washed twice again in flow cytometry buffer and recorded on a Bio-Rad ZE5 Cell Analyzer, or on a BD Fortessa, X20, or LSR flow cytometer.

For reactivity assays using antigen-loaded organoids, organoids were dissociated to single cells, and incubated in RPMI medium (without serum) with 10 μg/mL NY-ESO-1 peptide (SLLMWITQC, PepScan) or MART-1 peptide (ELAGIGILTV, Proteogenix) for 30′ at 37°C. Tumor cells were washed twice in PBS, resuspended in T cell medium and used for reactivity assays as described above.

For MHC-I blocking assays, tumor cells were pre-incubated with 50 μg/mL W6/32 MHC-I blocking antibody (Cell Services, the Francis Crick Institute, London, UK) for 30′ at 37°C before addition of T cells. Antibody remained present throughout the co-culture.

For MICA/B blocking assays, tumor cells were first loaded with NY-ESO-1 peptide, followed by pre-incubation for 30′ at 37°C with either 10 μg/mL MICA/B blocking antibodies (clone 6D4) or IgG2 isotype control (both BioLegend). Co-cultures were performed in the presence or absence of blocking or control antibodies.

NK cell reactivity assays

Two days before co-culture with organoids, NK cells were thawed and cultured with 10 ng/mL IL15 (Peprotech, #200-15) at a concentration of 1–2*10^6 cells in T cell medium. For co-cultures, NK cells were combined with dissociated tumor cells at a 2:1 ratio in T cell medium and plated at 2.5*10^4 NK cells/well in a U-bottom 96-well plate. After 24 h of co-culture, 100 μL supernatant was collected for cytokine analysis (see below), and cells were washed twice in flow cytometry buffer and stained with the following in flow cytometry buffer for 30′ at 4°C: anti-CD3-BB700 (BD Biosciences; SK7; 1:200 dilution), anti-CD16-AF700 (BioLegend; 3G8; 1:40), anti-CD56-BV605 (BioLegend; 5.1H11; 1:200), anti-CD137-PE (BD Biosciences; 4B4-1; 1:30), and live/dead fixable near-IR dead cell dye (Invitrogen; 1:200). Cells were washed twice again in flow cytometry buffer and recorded on a BD Fortessa flow cytometer.

Cytometric bead array (CBA)

Supernatant of co-culture assays was stored at −80°C until use. A 96-well U-bottom plate was washed once with CBA buffer (PBS supplemented with 0.1% BSA and 0.5 mM EDTA). 10 μL supernatant was added to each well and combined with 0.2 μL IFNg capture beads (CBA IFNg flex set, BD Biosciences) diluted in 10 μL CBA buffer, mixed for 5′ on an orbital shaker and incubated for 1 h at room temperature. 0.2 μL/well of IFNg detection antibody diluted in 10 μL CBA buffer was then added to each well, followed by mixing for 5′ on an orbital shaker and incubation for 2 h at room temperature. Fluorescence intensity was recorded on a BD Fortessa or LSR flow cytometer, with an IFNg standard curve as an internal reference. Data was interpolated to the standard curve using GraphPad Prism v10.0.3 and values below the interpolation range set to zero.

HLA class I and PD-L1 surface staining

Organoids were stimulated with 20 ng/mL IFNg for 48 h or left unstimulated before dissociation to single cells using accutase. Cells were washed twice in flow cytometry buffer and stained with the following antibodies (all 1:100 dilution) for 30′ at 4°C: anti-HLA-A2-APC (BB7.2, BD Biosciences), anti-HLA-ABC-PE (G46–2.6, BD Biosciences), PD-L1-APC (MIH-1, eBioscience), or IgG1 κ-APC (eBioscience) or IgG1 κ-PE isotype controls (BD Biosciences). (Invitrogen). Cells were washed twice again in flow cytometry buffer, stained with 1 μg/mL DAPI (Thermo Fisher) and recorded on a BD Fortessa, X20 or LSR flow cytometer.

NOA1 silencing

For siRNA-mediated knockdown of NOA1, organoids were dissociated to single cells using accutase and resuspended at 5*10^5 cells/1.5 mL MBM and plated at 1.5 mL per well in 6-well plates. Two separate microcentrifuge tubes were prepared for each transfection, each with 250 μL Opti-MEM (Gibco). 7.5 μL Lipofectamine RNAiMAX (ThermoFisher Scientific) was added to one tube, and 2 μL NOA1 (ThermoFisher, siRNA ID 147930) or control siRNA (Silencer negative control No. 01 siRNA, ThermoFisher) from 50 μM stock to the other tube, for a final concentration of 50 nM in 2 mL. Both tubes were incubated at room temperature for 5 min, mixed and incubated for an additional 15 min before adding 500 μL dropwise to each well (1.5 mL) of dissociated organoids. After centrifugation for 1 h at 100 g, organoids were cultured for 48 h at 37°C before continuing with organoid – T cell co-culture assays as described above. Knockdown efficiency was confirmed by RT-qPCR (see below).

RT-qPCR

To determine CTAG1B (NY-ESO-1) RNA expression, RNA and DNA were extracted with AllPrep DNA/RNA kit (Qiagen) according to manufacturer's instructions. 1 μg of RNA was reverse transcribed using the High-Capacity complementary DNA Reverse

Transcription Kit (ThermoFisher Scientific) according to manufacturer's instructions. CTAG1B (NY-ESO-1) (FWD: GCTTGAGTTC TACCTCGCCA; REV: ATGTTGCCGGACACAGTGAA) RNA expression was measured by qPCR using Fast SYBR Green Master Mix (ThermoFisher Scientific) on a LightCycler 480 (Roche). HPRT (FWD: AGCCAGACTTTGTTGGATTTG; REV: TTTACTGGCGATG TCAATAAG), TBP (FWD: CGGCTGTTTAACTTCGCTTC; REV: CACACGCCAAGAAACAGTGA) and UBC (FWD: ATTTGGGTCG CGGTTCTTG; REV: TGCCTTGACATTCTCGATGGT) were used as reference genes.

To determine NOA1 expression, RNA was isolated using RNeasy mini kit (Qiagen). 300 ng RNA was reverse transcribed using Maxima First Strand cDNA Synthesis Kit (ThermoScientific). NOA1 (FWD: CCTGCAGGGAAATCAGTCAG, REV: TCCACCCAT TGGAATCTGGA) RNA expression was measured by qPCR using a SensiFAST SYBR Hi-ROX kit (Meridian Bioscience) on a QuantStudio 3 (ThermoFisher) using GAPDH (FWD: TTAAAAGCAGCCCTGGTGAC, REV: CTCTGCTCCTCCTGTTCGAC) as reference gene.

Lentivirus production

HEK293T cells were transfected with standard PEI method. Briefly, cells were plated in a 6 cm ∅ dish in DMEM Glutamax (Gibco, Invitrogen) supplemented with 10% FBS (Gibco, Invitrogen) and 100 U/mL pencillin / 100 μg/mL streptomycin. When cells reached 90% confluency, they were transfected with the following transfection mix: 1 mL of Opti-MEM (Gibco, Invitrogen) containing 16.5 μL of PEI (1 mg/mL, pH 4.5, Polysciences), 1.25 μg of pCMV-ΔR8.2-dvpr (Addgene, #8455) plasmid DNA,[39] 0.415 μg of pCMV VSV-G (Addgene, #8454) plasmid DNA, and 2.85 μg of pLVX-CMV-CTAG1B (NY-ESO1)-IRES-ZsGreen, or pLVX-CMV-Stuffer-IRES-ZsGreen_empty control plasmid DNA (both from Manuel Varas, San Sebastian University, Chile). 16 h post-transfection, media was replaced with DMEM Glutamax (Gibco, Invitrogen) supplemented with 20% FBS (Gibco, Invitrogen) and 100 U/mL pencillin / 100 μg/mL streptomycin. Viral supernatant was collected 48 and 72 h post-transfection. Supernatant from the 48 h collection was kept at 4°C for 24 h and mixed with the 72 h supernatant. The mix was then centrifuged at 300 g for 5 min at room temperature, the supernatant was collected, avoiding contact with any visible pellet, and immediately filtered with a 0.45 μm low-adhesion filter (Merck Millipore) to remove any cell debris. Viral supernatant was either used fresh for lentiviral transduction or stored at −80°C.

CTAG1B (NY-ESO-1) transduction of organoids

Organoids were dissociated to single cells with accutase and resuspended at $1*10^6$ cells/mL in DMEM/F12 medium supplemented with 100 U/mL pencillin / 100 μg/mL streptomycin. Tumor cells were combined 1:1 with 3x diluted NY-ESO-1 lentivirus (pLVX-CMV-CTAG1B (NY-ESO1)-IRES-ZsGreen) or control virus (pLVX-CMV-Stuffer-IRES-ZsGreen_empty) in the presence of 8 μg/mL polybrene (Merck Millipore) and 10 μM Y-27632. Cells were plated at $1*10^6$ cells/well in a 12-well plate, centrifuged for 1 h at 100 g and incubated overnight at 37°C. Cells were washed in PBS and plated in BME for organoid formation as described above. Transduced organoids were selected based on puromycin resistance and transduction efficiency was monitored using flow cytometry based on co-expression of the fluorescent marker ZsGreen.

DNA sequencing

DNA and RNA was extracted from organoid samples or expanded TIL (as germline reference) with AllPrep DNA/RNA kit (Qiagen) according to manufacturer's instructions. Exome capture was performed using the Twist Fast Hybridization Target enrichment protocol on libraries prepared with the NebNext Ultra II DNA library Prep Kit (NEB), starting from over 200 ng of genomic DNA, following the manufacturer's instructions, and using the following key reagents (all Twist Bioscience): Human Core exome panel, Twist Universal Blockers, Twist Fast Hybridisation Reagents, and Twist Fast Wash Buffers. Samples were 100 bp paired-end sequenced on a NovaSeq at the Genomics Facility at the Francis Crick Institute, London, UK, with an aimed coverage of 300x for regional organoid lines, and 50x for clonal organoid lines and germline samples. Protocols for sequencing of primary tumor regions from TRACERx samples have been previously reported.[10]

Genomic analysis

DNA sequencing data was processed using a core pipeline which has been previously described in detail.[38] Phylogenetic trees were generated using the conipher R package (v2.1.0).[40] Specifically, we first performed mutational clustering using conipher (flags: –min_cluster_size 3, otherwise default parameters were used), we then generated trees using conipher on the clustered mutations (flags: –multi_trees FALSE, otherwise default parameters were used). For patient 3, the default tree resulted in the absence of a mutational cluster from the tree which was manually added after data curation. Trees were annotated with non-synonymous exonic mutations in lung cancer driver genes[10] and a manually curated list of genes relevant for immune control (Table S7). Plots showing hierarchical clustering of total copy number profiles were generated using seaborn.clustermap (v0.12.2, https://seaborn.pydata.org/generated/seaborn.clustermap.html).[41] Total copy number calls were generated using the Refphase R package (v0.3.2).[42] Upset plots for the visualization of mutation set overlap between regional or clonal organoids were generated with the upsetplot python package (v0.8.0; https://upsetplot.readthedocs.io/en/stable/).[43] MHC Hammer was run with default parameters to determine the presence of HLA LOH.[44] Analyses of mutational burden are based on the number of exonic non-synonymous single nucleotide variants (SNV) or insertion/deletion mutations (indel) per sample. Patient-specific HLA haplotype predictions were obtained using HLA-HD (version 1.2.1).[45] Computation of mutational and copy number distance have been previously described in detail.[38] In brief, the mutational distance between two regions is large if few mutations are shared, or those mutations occur at very different frequencies.

Truncal mutations are included for the calculation of mutational distance. Copy number distance is large if gains/losses of segments relative to ploidy diverge between regions. Mutation distance (but not copy number distance) is limited between 0 and 1.

To identify neoantigens, NetMCHpan4.1[46] was run on 9–11 neopeptides derived from nonsynonymous mutations across the organoids, taking into account patient-specific HLA types. A cutoff of 2 in the eluted ligand rank was applied to define whether a peptide is bound to a specific HLA type. An observed nonsynonymous mutation is deemed a neoantigen binding to a specific HLA if at least one of its neopeptides is considered a binder.

RNA sequencing

Organoids were stimulated with 20 ng/mL IFNg for 24 h or left unstimulated prior to isolation from BME by washing in ice-cold PBS and RNA extraction using an AllPrep DNA/RNA kit (Qiagen) according to manufacturer's instructions. Library prep was performed with 100–500 ng RNA using a KAPA mRNA polyA HyperPrep kit (Roche). Samples were 100 bp single read sequenced on a NovaSeq at the Genomics Facility at the Francis Crick Institute, London, UK.

Differential gene expression analysis

Differential gene expression analysis was performed using a similar approach as described previously,[38] with the following adaptations. Limma-voom (v.3.54.1)[47] was used to determine expression differences between organoid sublines of different immune classes: hot (R3, R4) and cold (R2, R5) for patient 1, and hot (C24, C26), intermediate (C13, C305) and cold (C304, C308) for patient 2. Treatment status (IFNg pre-treatment or not) was included as a term in an interaction model with immune class. Region (patient 1) or clone (patient 2) was taken as a blocking factor, by performing within-region or within-clone expression correlations and including them within the voom model estimate based on the duplicateCorrelation function. Raw p values were adjusted using the Benjamini-Hochberg (FDR) method, and genes with an adjusted p value <0.05 and an >1 absolute log2 fold change in expression were considered significant (>2 for focused analysis of immune evasion genes).

Principal component analysis was performed on $\log_2$ transformed count data normalized for library size using the rlog function from the DESeq2 package (v1.38.3)[48] and the prcomp R function. Trimmed mean of M-value normalized count data was generated using edgeR (v3.40.2).[49] Expression of immune evasion genes was performed by filtering differential expression data between hot and cold organoids against a pre-defined list of immune evasion genes (Table S7).

Gene set enrichment analyses were performed on the differentially expressed genes using the t statistic from the limma results table as a score to rank genes. The function fgsea from the R package fgsea (v1.16.0)[50] was run with default parameters on all 50 hallmarks from the MSigdb database.[56] Genesets from the hallmarks were obtained using the function msigdbr from the msigdbr (v7.5.1) package (Dolgalev, https://igordot.github.io/msigdbr/).

The induction of interferon stimulated genes was determined for a selection of genes from the "hallmark_response_to_interferon_gamma" gene set from the Msigdb database.[56,57] A metagene was constructed based on the scaled average expression of all genes from this gene set, using the scale function from R version 4.2.2.

Bulk T cell receptor beta chain (TCRb) sequencing

For unexpanded TIL from patient 2 (R7) and expanded TIL from patient 1 (R2 or R3/4/5 combined), bulk T cell receptor beta chain sequencing was performed as previously described.[51,58] Briefly, whole RNA was extracted from NSCLC tumor samples (patient 2) or expanded TIL sorted for $CD8^+$ T cells (patient 1), reverse transcribed, ligated at the 3′ end with a single-stranded oligonucleotide barcode, and amplified by qPCR prior to Illumina sequencing. The inclusion of a unique molecular identifier in each barcode enabled rigorous correction for PCR and sequencing errors. TCR identification, error correction and CDR3 extraction were performed on sequenced reads using a custom suite of analysis tools: https://github.com/innate2adaptive/Decombinator.[51] TCR clones were defined by the unique combination of V and J genes and CDR3 amino acid sequences.

For patient 2, genomic DNA was extracted from expanded TIL (R7) and bulk TCRb sequencing was performed by Adaptive Biotechnologies and analyzed using the immunoSEQ analyzer platform.

Single cell RNA and TCR sequencing

For single cell RNA sequencing on patient 2 unexpanded TIL, cryopreserved TILs were enriched for T cells based on flow cytometry assisted cell sorting (FACS). Library preparation was performed using the Chromium Next GEM Single-cell 5′ kit v2 (10x Genomics). Raw sequencing data were processed using Cell Ranger v6.0 with default settings (https://support.10xgenomics.com/single-cell-gene-expression/software/pipelines/latest/what-is-cell-ranger). Reads were aligned to the human reference genome GRCh38. Processed single-cell RNA data was analyzed with custom in-house scripts in python (v3.8) using scanpy (v1.9.1, https://scanpy.readthedocs.io/).[52] For visualization of gene expression, a uniform manifold approximation and projection embedding was calculated using principal components calculated using highly variable genes (excluding mitochondrial, ribosomal, haemoglobin-encoding and T cell receptor V and J genes). Cells were scored with gene signatures for expression of CD3 (*CD3D*, *CD3E*, *CD3G*) or published signatures for $CD8^+$ neoantigen-reactive (neoTCR8),[17] stem-like exhausted,[59] or exhausted[60] T cells using "scanpy.tl.score_genes()".

The Cell Ranger VDJ filtered_contig_annotations output was used to define TCR clones and connect TCR clone identities to gene expression in the single-cell dataset. TCR clones were matched between the bulk T cell receptor beta chain sequencing and the single cell TCR sequencing dataset through sharing of V and J genes and CDR3 amino acid sequences (identical matches were made when using the CDR3 nucleotide sequence). Each bulk TCR chain for the dominant (Clone #1) and subdominant (Clone #2) clones in

expanded TIL (Figure S1G) matched a single single-cell TCR clone. Comparison of gene expression in single cell TCR sequencing data was performed using an unpaired one-sided Wilcoxon signed-rank test, as implemented in the R package ggpubr, without correction for multiple testing.

QUANTIFICATION AND STATISTICAL ANALYSIS

Statistical testing was performed using R version 4.2.2 or Prism (v10.0.3). Replicates represent biological replicates (from independent experiments using organoid lines of different passage or processed on different moments), unless otherwise indicated. For the comparison of multiple conditions, when repeated measurements were available, a repeated-measures ANOVA was used. Repeated measures ANOVA cannot handle missing values. When there were missing values, we analyzed the data instead by fitting a mixed model as implemented in GraphPad Prism. This mixed model uses a compound symmetry covariance matrix, and is fit using Restricted Maximum Likelihood (REML). In the absence of missing values, this method gives the same p values and multiple comparisons tests as repeated measures ANOVA. In the presence of missing values, the results can be interpreted like repeated measures ANOVA. Ordinary one-way ANOVA was used if no repeated measurements data was available. Unless otherwise indicated, all experimental conditions were compared in a pairwise manner, and Tukey's multiple comparison correction was applied. Only significant comparisons are plotted. For comparison of two conditions, two-sided paired t-tests were used. Bar graphs show mean ± s.e.m. and circles indicate individual data points, unless otherwise indicated in Figure legends. Additional details for statistical tests are indicated in figure legends. Statistical details for organoid differential expression analysis and TCR sequencing are indicated under the relevant Methods subheadings. Statistical significance indicated by asterisks: $^{*}p < 0.05$; $^{**}p < 0.01$; $^{***}p < 0.001$; $^{****}p < 0.0001$.